

# Lockhart with a twist: modelling cellulose microfibril deposition and reorientation reveals twisting plant cell growth mechanisms

Jeevanjyoti Chakraborty<sup>a,b</sup>, Jingxi Luo<sup>a</sup>, Rosemary J. Dyson<sup>a,\*</sup>

<sup>a</sup>*School of Mathematics, University of Birmingham, Birmingham B15 2TT, UK*

<sup>b</sup>*Indian Institute of Technology Kharagpur, Kharagpur, 721302, West Bengal, India*

---

## Abstract

Plant morphology emerges from cellular growth and structure. The turgor-driven diffuse growth of a cell can be highly anisotropic: significant longitudinally and negligible radially. Such anisotropy is ensured by cellulose microfibrils (CMF) reinforcing the cell wall in the hoop direction. To maintain the cell's integrity during growth, new wall material including CMF must be continually deposited. We develop a mathematical model representing the cell as a cylindrical pressure vessel and the cell wall as a fibre-reinforced viscous sheet, explicitly including the mechano-sensitive angle of CMF deposition. The model incorporates interactions between turgor, external forces, CMF reorientation during wall extension, and matrix stiffening. Using the model, we reinterpret some recent experimental findings, and reexamine the popular hypothesis of CMF/microtubule alignment. We explore how the handedness of twisting cell growth depends on external torque and intrinsic wall properties. Overall, this study provides a unified mechanical framework for understanding left- and right-handed twist-growth as seen in many plants.

*Keywords:* twist growth, cell wall anisotropy, fibre reorientation, fibre-reinforced fluid, matrix stiffening

---

\*Corresponding author

Email addresses: [jeevan@mech.iitkgp.ac.in](mailto:jeevan@mech.iitkgp.ac.in) (Jeevanjyoti Chakraborty), [j.luo.5@bham.ac.uk](mailto:j.luo.5@bham.ac.uk) (Jingxi Luo), [r.j.dyson@bham.ac.uk](mailto:r.j.dyson@bham.ac.uk) (Rosemary J. Dyson)

## 1. Introduction

To attain a fundamental understanding of plant growth is an attractive frontier of developmental biology, as it can help to ensure that plants thrive in adverse climatic and agricultural environments (Lynch and Wojciechowski, 2015). It is therefore imperative to improve predictive capabilities and mechanistic insight for growth and morphogenesis based on findings of biological structure and function (Mirabet et al., 2011). Mathematical modelling holds the key to a quantitative framework for explaining and predicting plant growth phenomena across different scales: from cellular through tissue to organismic (Bruce, 2003; Ali et al., 2014; Jensen and Fozard, 2015). Here, we focus on the cellular level.

Plant cell growth can broadly be of two types: tip growth, where growth occurs at a tip of the cell; and diffuse growth, where growth occurs over the whole cell. In this work we focus on the latter. A common example of such diffuse growth is found in the primary root of *Arabidopsis thaliana*, predominantly within the elongation zone (EZ) of the root. We view the simplified structure of a cell as a pressure vessel which is approximately cylindrical, bounded by a viscous fluid sheet representing the cell wall. The cytoplasm imposes an internal turgor pressure, which acts on the cell wall to induce irreversible expansion and hence growth. The cell wall is reinforced by cellulose microfibrils (CMF) arranged in a hoop-like fashion within a ground matrix made of pectin and hemicellulose. The CMF reinforcement produces growth anisotropy, with significant expansion along the axial direction and little expansion in the radial direction (Baskin, 2005). The CMF can resist ground matrix mobility in the hoop direction, thereby preventing radial growth; they can also sustain high tensile forces and inhibit growth along their length (Somerville et al., 2004). The model presented here will incorporate all of the effects outlined above.

One of the simplest and most widely-used theoretical models of plant cell growth was devised by Lockhart (1965). According to the Lockhart equation, turgor pressure,  $P$ , can initiate growth (i.e. a positive relative elongation rate, or RER, for a cell of length  $l$  at time  $t$ ) only beyond a threshold value  $Y$ , and the growth reflects a viscoplastic behaviour through an extensibility

parameter  $\Phi$ , such that

$$\text{RER} \equiv \frac{1}{l} \frac{dl}{dt} = \Phi (P - Y), \quad \text{for } P > Y. \quad (1)$$

Some work has been done to express the threshold value  $Y$  and the extensibility parameter  $\Phi$  in terms of structural components of the cell (Passioura and Fry, 1992; Veytsman and Cosgrove, 1998; Dyson et al., 2012); see Smithers et al. (2019) for more details.

A major defect of the Lockhart equation (1) is its globalness: it does not link biological structure to local growth mechanics. Alternatives to, or variations on, the Lockhart model have been proposed. Ortega (1985) augmented the Lockhart equation to include elastic effects. More recently, Dyson and Jensen (2010) adopted a bottom-up approach, modelling the structural components of the cell and properly accounting for stresses based on fundamental mechanical principles. The proposed fibre-reinforced viscous fluid model of the cell wall, with particular focus on the orientation of the CMF, was similar in spirit to an earlier work for tip growth by Dumais et al. (2006). Progress has also been made in upscaling cell-level properties to the tissue-level in order to study organ elongation and bending (Dyson et al., 2014). Furthermore, Huang et al. (2012, 2015) developed a rigorous hyperelastic-viscoplastic model of cell growth incorporating the effects of reorienting microfibrils, wall loosening and hardening, and anisotropic material properties. These studies built on a number of previous growth models that had employed elasticity theories of shells and membranes (Boudaoud, 2003; Goriely and Tabor, 2008). A detailed critique and comparison of these and other models of growth of walled cells may be found in some excellent reviews (Geitmann and Ortega, 2009; Ortega and Welch, 2013; Smithers et al., 2019).

Despite their broad scope, these models cannot capture all aspects of biological reality, and one such aspect of great importance is helical or twisting growth. Understanding organ-level twist growth matters because of its ecological and economic implications. For example, helical mutants of crops tend to be smaller than straight-growing wild-types; on the flipside, twisting roots may push through soil more efficiently (Chen et al., 2003). Since single-cell twisting can translate into organ helicity, models of twisting cell growth may serve as proxies for organ-level phenomena (Schulgasser and Witztum, 2004). Indeed, helical organ growth may be a relaxation mechanism to resolve the conflict between single cell tendencies to twist and cell-cell adhesion

forces (Verger et al., 2019). Yet, a model of cellular twist growth is currently lacking. The mechanical model that we present here incorporates left- and right-handed twist under a unified framework, responding to the fact that the two orientations are not pathway-separated (Buschmann and Borchers, 2019). The model integrates cell wall components, since handedness may be an intrinsic property of the cell wall (Landrein et al., 2013) and pectin may counteract the cell wall chirality (Saffer et al., 2017). The stiffening of pectin gels in the ground matrix, which may be a function of pectin methylesterases, is also considered (Peaucelle et al., 2015).

In this study, we build on and extend the formulation of Dyson and Jensen (2010) to develop a more general framework incorporating dynamic evolution of CMF deposition angle and matrix stiffening effects. A temporally varying deposition angle is compatible with varying fibre orientation across the cell wall thickness, which can result from different extents to which reorientation occurs during cell expansion (Anderson et al., 2010). Crucially, we show that the interaction between orientation variations and mechanical forces regulates twisting growth behaviour.

The rest of this paper is organised as follows. In Section 2, we present our governing equations in the most general form. We describe the axisymmetric geometry to model the cell, set up the co-ordinate system, specify kinematic constraints, and present the nondimensionalisation. In Section 3, we simplify the system of equations through asymptotic techniques, detailing how to obtain the conditions for constant radius of the cell and constant thickness of the cell wall. In Section 4, we summarise the model, presenting dynamical equations for cell elongation, cell twist and fibre re-orientation, and provide a brief analysis of the system including constraints on the parameter space. We also describe the types of initial and boundary conditions that will be imposed. In particular, we describe two choices of CMF-deposition regime, both of which are justified by experimental observations. We then solve the equations numerically and present results in Section 5. We investigate the effect on growth of various model parameters, including viscosity coefficients, external torque, and allowing the isotropic viscosity coefficient to evolve in time. The latter effect mimics matrix stiffening. Finally, in Section 6, we draw conclusions and highlight the biological implications of our results.

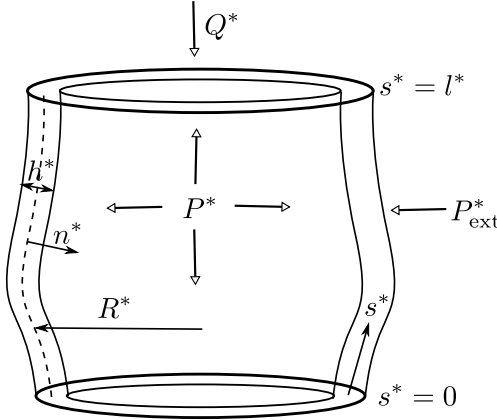


Figure 1: Model geometry of a single cell whose wall is represented as an axisymmetric sheet held between two rigid plates.

## 2. Model outline

We model the cell as an axisymmetric structure surrounded by a sheet of viscous, incompressible fluid which represents a permanently yielded cell wall (Figure 1). The sheet is attached to rigid end plates and subjected to a uniform internal pressure  $P^*$ . All external effects due to neighbouring cells are captured through a longitudinal pressure,  $Q^*$ ; a radial compressive pressure,  $P_{\text{ext}}^*$ ; and a torque  $\Sigma^*$  applied to the top end of the cell. The bottom end is assumed fixed. To simplify the formulation without losing generality, we take  $P_{\text{ext}}^* = 0$ , implying that all other pressures are represented with respect to the external compressive pressure. Thus, it is the direct action of  $P^*$  that induces cell growth. This growth would lead to the thinning of the cell wall; to compensate, new material is continually deposited on the inner surface of the cell wall, which we model by an explicit boundary condition.

### 2.1. Governing equations

Conservation of mass under the assumption of incompressibility is given by

$$\nabla^* \cdot \mathbf{U}^* = 0, \quad (2)$$

where  $\mathbf{U}^*$  is the fluid velocity. We will encode CMF deposition through a kinematic boundary condition (to be detailed later). Conservation of mo-

mentum is given by

$$\nabla^* \cdot \boldsymbol{\sigma}^* = 0, \quad (3)$$

where  $\boldsymbol{\sigma}^*$  is the Cauchy stress tensor.

The stress tensor is related to the velocity through an appropriate constitutive relation, which depends on the material make-up of the cell wall. Here, we model the cell wall as a homogeneous material (denoting the pectin matrix together with the hemicellulose links) reinforced by fibres (denoting the CMF). We consider a single family of fibres with a director field  $\mathbf{a}$ , such that  $|\mathbf{a}| = 1$ . To model this fibre-reinforced cell wall material, we choose a phenomenological constitutive relation displaying transverse isotropy along the director field (Ericksen, 1960),

$$\begin{aligned} \boldsymbol{\sigma}^* = & -p^* \mathbf{I} + 2\mu_0^* \mathbf{e}^* + \mu_1^* \mathbf{a} \otimes \mathbf{a} + \mu_2^* \zeta^* (\mathbf{a} \otimes \mathbf{a}) \\ & + 2\mu_3^* \{ \mathbf{a} \otimes (\mathbf{e}^* \mathbf{a}) + (\mathbf{e}^* \mathbf{a}) \otimes \mathbf{a} \}, \end{aligned} \quad (4)$$

where  $p^*$  is the fluid pressure,  $\mathbf{I}$  is the identity tensor,  $\mu_0^*$ ,  $\mu_2^*$ , and  $\mu_3^*$  are viscosity coefficients,  $\mu_1^*$  is any active tension along the fibre direction, and  $\zeta^* = \mathbf{a}^T \mathbf{e}^* \mathbf{a}$  is the strain rate in the fibre direction with  $\mathbf{e}^* = (\nabla^* \mathbf{U}^* + \nabla^* \mathbf{U}^{*T})/2$  being the rate-of-strain tensor. The constitutive relation for an incompressible isotropic fluid can be recovered from (4) by setting  $\mu_1^* = \mu_2^* = \mu_3^* = 0$ , so  $\mu_0^*$  can be interpreted as the isotropic component of the matrix viscosity modified by the fibre volume fraction. Since the third term on the right-hand side of (4) is independent of  $\mathbf{e}^*$ , it contributes to the presence of a stress even when the velocity is zero. Additionally, since this term involves only the director field, the viscosity coefficient  $\mu_1^*$  represents the stress in the fibres; this stress can only be a tensile one because no stress is induced in the fibres under compression. The coefficients  $\mu_2^*$  and  $\mu_3^*$  are interpreted by considering two-dimensional deformations in the plane of the fibres. Parallel to the fibre direction, we have the extensional viscosity  $\mu_{\parallel}^* = \mu_0^* + (\mu_2^* + 4\mu_3^*)/2$ , while orthogonal to the fibre direction, we have  $\mu_{\perp}^* = \mu_0^*$ ; furthermore, the shear viscosity is  $\mu_s^* = \mu_0^* + \mu_3^*$  parallel to the fibre direction. Since  $\mu_2^*$  contributes only to  $\mu_{\parallel}^*$ , it is interpreted as an extensional viscosity; and  $\mu_3^*$  serves to distinguish between  $\mu_{\perp}^*$  and  $\mu_s^*$ . Since  $\mu_0^*$  has been recognised as the isotropic contribution,  $\mu_3^*$  can be interpreted as the anisotropic contribution to the shear viscosity. For further discussions, see Holloway et al. (2018).

The model allows all  $\mu_i^*$  to vary in space and time. In particular, we focus here on solutions where  $\mu_0^*$  varies spatial-temporally, encoding changes in

pectin or hemicellulose. To model this effect, we employ a minimal evolution equation,

$$\frac{\partial \mu_0^*}{\partial t^*} + (\mathbf{U}^* \cdot \nabla^*) \mu_0^* = \alpha^*, \quad (5)$$

where  $\alpha^*$  is some constant rate of matrix stiffening.

The director field itself evolves according to the transport equation (Green and Friedman, 2008; Dyson et al., 2016),

$$\frac{\partial \mathbf{a}}{\partial t^*} + (\mathbf{U}^* \cdot \nabla^*) \mathbf{a} + \zeta^* \mathbf{a} = (\mathbf{a} \cdot \nabla^*) \mathbf{U}^*. \quad (6)$$

whereby the director field is convected, stretched and reoriented by the wall material.

The governing equations (2–6) describe the dynamics of a cell. Clearly, boundary and initial conditions are required for the system; we detail these in Section 4.1, after simplifications of the equations. The general framework we have presented allows us to investigate a rich array of phenomena, by prescribing boundary conditions which are rooted in biological reality. The novel ability to make these boundary conditions explicit and spatio-temporally varying gives us a much larger toolbox with which to probe plant growth mechanics.

## 2.2. Geometric simplification

We proceed to express the model in body-fitted coordinates, following van de Fliert et al. (1995) and Dyson and Jensen (2010), so that we can exploit the slender geometry of the cell wall later. We use a curvilinear coordinate system in the fluid sheet, with the right-handed coordinate 3-tuple  $(s^*, \theta, n^*)$  (Figure 1). Here,  $s^*$  denotes the arclength measured from the base plate along the centre-surface of the fluid sheet;  $\theta$  is the azimuthal angle increasing anticlockwise as viewed from the top; and  $n^*$  is the distance from the centre-surface taken to be positive in the inward normal direction. We assume that the cell is axisymmetric about the longitudinal axis, so that  $\partial/\partial\theta \equiv 0$ . At any point  $(s^*, \theta)$  on the centre-surface of the sheet, the distance from the longitudinal axis of the cell is the cell radius,  $R^*(s^*, t^*)$ , and the fluid sheet thickness is  $h^*(s^*, t^*)$ . Since  $s^*$  and  $n^*$  are fitted to the fluid sheet, we measure the flow using the velocity  $\mathbf{u}^* = \mathbf{U}^* - \mathbf{v}^*$  relative to the velocity  $\mathbf{v}^*$  of the

centre-surface. The components  $v_s^*$ ,  $v_\theta^*$ , and  $v_n^*$  of this centre-surface velocity measured along the three base vectors  $\mathbf{e}_s$ ,  $\mathbf{e}_\theta$  and  $\mathbf{e}_n$  respectively, satisfy the kinematic constraints

$$0 = \frac{\partial v_s^*}{\partial s^*} - \kappa_s^* v_n^*, \quad (7a)$$

$$\frac{\partial R^*}{\partial t^*} = v_s^* \frac{\partial R^*}{\partial s^*} - R^* \kappa_\theta^* v_n^*, \quad (7b)$$

$$v_\theta^* \frac{\partial R^*}{\partial s^*} = R^* \frac{\partial v_\theta^*}{\partial s^*}, \quad (7c)$$

where the azimuthal and axial curvatures of the centre-surface are given by

$$\kappa_\theta^* = \frac{\Delta^*}{R^*}, \quad \kappa_s^* = -\frac{1}{\Delta^*} \frac{\partial^2 R^*}{\partial s^{*2}}, \quad (8)$$

with  $\Delta^* = (1 - (\partial R^* / \partial s^*)^2)^{1/2}$ . See Appendix A of Dyson and Jensen (2010) for details.

Since we are using a curvilinear co-ordinate system, the contravariant components of the vectors and tensors must be converted throughout to the physical components using the scaling factors

$$l_s = 1 - \kappa_s^* n^*, \quad l_\theta^* = R^* (1 - \kappa_\theta^* n^*), \quad l_n = 1, \quad (9)$$

where  $l_s$  and  $l_n$  are dimensionless.

Finally, we assume  $a_n = 0$ , i.e. the fibres lie in the tangential plane of the fluid sheet, so that  $a_s = \sin \phi$  and  $a_\theta = \cos \phi$  with  $\phi$  being the angle made by a fibre with the horizontal. We let  $\phi$  take values in  $-\pi/2 \leq \phi \leq \pi/2$ , because the system must be invariant under  $\phi \rightarrow \phi + \pi$ . Crucially, a fibre with  $0 < \phi < \pi/2$  has right-handed helicity when viewed from outside the cell, whereas  $-\pi/2 < \phi < 0$  corresponds to left-handed helicity. We will use the  $a_s$ ,  $a_\theta$  and the  $\phi$  notation interchangeably, depending on context.

### 2.3. Nondimensionalisation

We nondimensionalise the system using the following scalings:

$$\left. \begin{aligned} \{R^*, s^*, l^*, l_\theta^*\} &= R_0^* \{R, s, l, l_\theta\}, & \{n^*, h^*\} &= h_0^* \{n, h\}, & t^* &= \frac{\epsilon M_0^*}{P_0^*} t, \\ \{\mathbf{U}^*, \mathbf{u}^*, \mathbf{v}^*, \mathcal{F}^*\} &= \frac{R_0^* P_0^*}{\epsilon M_0^*} \{\mathbf{U}, \mathbf{u}, \mathbf{v}, \mathcal{F}\}, & \{\mathbf{e}^*, \zeta^*\} &= \frac{P_0^*}{\epsilon M_0^*} \{\mathbf{e}, \zeta\}, \\ \{\boldsymbol{\sigma}^*, p^*, \mu_1^*, \alpha^*\} &= \frac{P_0^*}{\epsilon} \{\boldsymbol{\sigma}, p, \mu_1, \alpha\} & \{\mu_0^*, \mu_2^*, \mu_3^*\} &= M_0^* \{\mu_0, \mu_2, \mu_3\}, \\ \{P^*, Q^*\} &= P_0^* \{P, Q\}, & \Sigma^* &= R_0^* P_0^* \Sigma, & \{\kappa_s^*, \kappa_\theta^*\} &= \frac{1}{R_0^*} \{\kappa_s, \kappa_\theta\}, \end{aligned} \right\} \quad (10)$$

where  $R_0^*$  is the initial radius of the cell,  $h_0^*$  the initial thickness of the cell wall,  $M_0^*$  the initial viscosity of the matrix, and  $P_0^*$  the initial turgor pressure, all of which are assumed to be uniform; the aspect ratio,  $\epsilon = h_0^*/R_0^*$ , is assumed small ( $\epsilon \ll 1$ ). Upon nondimensionalisation, the governing equations (2–6) retain their form, as do (7) and (8). For  $l_s$  and  $l_\theta$ , we have

$$l_s = 1 - \epsilon \kappa_s n, \quad l_\theta = R(1 - \epsilon \kappa_\theta n). \quad (11)$$

Isolating the small parameter  $\epsilon$  enables us to simplify the system further, to such an extent that we can compute approximate solutions.

### 3. Asymptotic simplifications

Exploiting the small ratio  $\epsilon$  between cell wall thickness and cell radius, we consider asymptotic expansions of the form

$$\mathcal{E} \sim \mathcal{E}^{(0)} + \epsilon \mathcal{E}^{(1)} + \epsilon^2 \mathcal{E}^{(2)} \dots, \quad (12)$$

which lead to simplified equations for the dynamics of the fluid sheet and the reinforcing fibres. The presence of the fibres within the fluid does not alter the crucial simplifying leading-order findings as previously determined by Howell (1994) and van de Fliert et al. (1995), namely that of plug flow ( $\mathbf{U}^{(0)} = \mathbf{U}^{(0)}(s, t)$ ), and no normal fluid flow relative to the centre-surface ( $u_n^{(0)} = 0$ ). We proceed to follow van de Fliert et al. (1995) and Dyson and

Jensen (2010) for parts of the derivation, whilst incorporating the effects of varying fibre angle across the thickness of the sheet.

We first derive the integrated incompressibility equation, systematically addressing contributions at various asymptotic orders, with new material deposition represented by (13). The asymptotic treatment leads naturally to the appropriate value of deposition rate required to maintain a constant cell wall thickness. Then, the development of the integrated momentum conservation and constitutive equations follows exactly from van de Fliert et al. (1995) and Dyson and Jensen (2010), so we use these equations without repeating the lengthy derivations here. Furthermore, we address the fibre transport equation through a proper asymptotic treatment which will result in a major difference with Dyson and Jensen (2010). We will impose conditions which ensure that both the cell radius  $R$  and cell wall thickness  $h$  remain constant and uniform. Our choice of nondimensionalisation immediately leads to these values being 1. The turgor pressure  $P$  is also taken as constant and uniform throughout this analysis, and thus could be set to 1. However we will retain  $R$ ,  $h$  and  $P$  in the first instance, for ease of interpretation.

### 3.1. Mass equation

At the  $n$ -boundaries of the fluid sheet, we prescribe kinematic conditions, with the influx of new material given by some deposition function  $\mathcal{F}^*$ :

$$u_n = \begin{cases} -\mathcal{F} + \frac{\epsilon}{2} \frac{\partial h}{\partial t} + \frac{\epsilon}{2l_s} \frac{\partial h}{\partial s} \left[ u_s + \frac{\epsilon h}{2} \left( \kappa_s v_s + \frac{\partial v_n}{\partial s} \right) \right], & n = \frac{h}{2}, \\ -\frac{\epsilon}{2} \frac{\partial h}{\partial t} - \frac{\epsilon}{2l_s} \frac{\partial h}{\partial s} \left[ u_s - \frac{\epsilon h}{2} \left( \kappa_s v_s + \frac{\partial v_n}{\partial s} \right) \right], & n = -\frac{h}{2}, \end{cases} \quad (13)$$

where  $u_n = U_n - v_n$  and  $u_s = U_s - v_s$ . Details may be found in Howell (1994) and van de Fliert et al. (1995).

In Appendix A, we show that the leading-order contribution to deposition  $\mathcal{F}^{(0)} = 0$ . Therefore the leading-order mass equation (2) is

$$\frac{\partial}{\partial t} (h^{(0)} R^{(0)}) + \frac{\partial}{\partial s} (h^{(0)} R^{(0)} u_s^{(0)}) = \mathcal{F}^{(1)} R^{(0)}. \quad (14)$$

### 3.2. Momentum equations

For notational convenience, we define, for generic variable  $\mathcal{E}$ , the integral over the cell wall thickness of the leading-order  $\mathcal{E}^{(0)}$ :

$$\overline{\mathcal{E}} \equiv \int_{-h/2}^{h/2} \mathcal{E}^{(0)} dn. \quad (15)$$

The leading-order momentum equations (3) are

$$\kappa_s^{(0)} \overline{\sigma}_{ss} + \kappa_\theta^{(0)} \overline{\sigma}_{\theta\theta} = P, \quad (16a)$$

$$\frac{\partial}{\partial s} \left( (R^{(0)})^2 \kappa_\theta^{(0)} \overline{\sigma}_{ss} \right) = PR^{(0)} \frac{\partial R^{(0)}}{\partial s}, \quad (16b)$$

$$\frac{\partial}{\partial s} \left( (R^{(0)})^2 \overline{\sigma}_{s\theta} \right) = 0, \quad (16c)$$

where  $\overline{\sigma}_{ss}$ ,  $\overline{\sigma}_{\theta\theta}$ , and  $\overline{\sigma}_{s\theta}$  are the stress components integrated over the thickness of the wall. In particular,  $\overline{\sigma}_{ss}$  gives the longitudinal tension within the wall,  $\overline{\sigma}_{\theta\theta}$  is the azimuthal tension, and  $\overline{\sigma}_{s\theta}$  is the tension caused by shear stresses. Here (16a), (16b), and (16c) represent, respectively, the conservation of momentum normal, longitudinal, and azimuthal to the fluid sheet.

### 3.3. Constitutive equations

The integrated components of the constitutive equation (4) at leading order are

$$\begin{aligned}\bar{\sigma}_{ss} &= 2\bar{\mu}_0 \left( 2 \frac{\partial u_s^{(0)}}{\partial s} + \frac{1}{R^{(0)}} \frac{DR^{(0)}}{Dt} \right) + \bar{\mu}_1 a_s^2 + \bar{\mu}_2 a_s^2 \zeta \\ &+ 4 \left( \bar{\mu}_3 a_s^2 \frac{\partial u_s^{(0)}}{\partial s} + \frac{1}{2} \bar{\mu}_3 a_s a_\theta \left( \frac{\partial u_\theta^{(0)}}{\partial s} - \frac{u_\theta^{(0)}}{R^{(0)}} \frac{\partial R^{(0)}}{\partial s} \right) \right),\end{aligned}\quad (17a)$$

$$\begin{aligned}\bar{\sigma}_{s\theta} &= \bar{\mu}_0 \left( \frac{\partial u_\theta^{(0)}}{\partial s} - \frac{u_\theta^{(0)}}{R^{(0)}} \frac{\partial R^{(0)}}{\partial s} \right) + \bar{\mu}_1 a_s a_\theta + \bar{\mu}_2 a_s a_\theta \zeta \\ &+ \bar{\mu}_3 \left( \frac{\partial u_\theta^{(0)}}{\partial s} - \frac{u_\theta^{(0)}}{R^{(0)}} \frac{\partial R^{(0)}}{\partial s} \right) + 2 \frac{\bar{\mu}_3 a_s a_\theta}{R^{(0)}} \left( \frac{DR^{(0)}}{Dt} + R^{(0)} \frac{\partial u_s^{(0)}}{\partial s} \right),\end{aligned}\quad (17b)$$

$$\begin{aligned}\bar{\sigma}_{\theta\theta} &= 2\bar{\mu}_0 \left( \frac{\partial u_\theta^{(0)}}{\partial s} + \frac{2}{R^{(0)}} \frac{DR^{(0)}}{Dt} \right) + \bar{\mu}_1 a_\theta^2 + \bar{\mu}_2 a_\theta^2 \zeta \\ &+ 4 \left( \frac{\bar{\mu}_3 a_\theta^2}{R^{(0)}} \frac{DR^{(0)}}{Dt} + \frac{1}{2} \bar{\mu}_3 a_s a_\theta \left( \frac{\partial u_\theta^{(0)}}{\partial s} - \frac{u_\theta^{(0)}}{R^{(0)}} \frac{\partial R^{(0)}}{\partial s} \right) \right),\end{aligned}\quad (17c)$$

where  $\bar{\mu}_0 = h$  if it is constant and uniform, due to our choice of nondimensionalisation.

### 3.4. Matrix stiffening

Equation (5) for the evolution of  $\mu_0$  at  $\mathcal{O}(1)$  reads

$$(u_n^{(0)} + v_n^{(0)}) \frac{\partial \mu_0^{(0)}}{\partial n} = 0, \quad (18)$$

and at  $\mathcal{O}(\epsilon)$ , we have

$$\frac{\partial \mu_0^{(0)}}{\partial t} + (u_s^{(0)} + v_s^{(0)}) \frac{\partial \mu_0^{(0)}}{\partial s} + (u_s^{(0)} + v_s^{(0)}) \frac{\partial \mu_0^{(1)}}{\partial n} + (u_s^{(1)} + v_s^{(1)}) \frac{\partial \mu_0^{(0)}}{\partial n} = \alpha. \quad (19)$$

### 3.5. Fibre angle evolution

We consider the nondimensionalised version of (6) and expand it in terms of the physical components to obtain, at  $\mathcal{O}(1)$ :

$$U_n^{(0)} \frac{\partial \phi^{(0)}}{\partial n} = 0, \quad (20)$$

and at  $\mathcal{O}(\epsilon)$ :

$$\begin{aligned} \frac{\partial \phi^{(0)}}{\partial t} + U_s^{(0)} \frac{\partial \phi^{(0)}}{\partial s} + U_n^{(0)} \frac{\partial \phi^{(1)}}{\partial n} + U_n^{(1)} \frac{\partial \phi^{(0)}}{\partial n} &= \sin \phi^{(0)} \cos \phi^{(0)} \frac{\partial u_s^{(0)}}{\partial s} \\ &- \sin^2 \phi^{(0)} \left( \frac{\partial u_\theta^{(0)}}{\partial s} - \frac{u_\theta^{(0)}}{R^{(0)}} \frac{\partial R^{(0)}}{\partial s} \right) - \frac{\sin \phi^{(0)} \cos \phi^{(0)}}{R^{(0)}} \frac{DR^{(0)}}{Dt}, \end{aligned} \quad (21)$$

$$\begin{aligned} \zeta^{(0)} &= \sin^2 \phi^{(0)} \frac{\partial u_s^{(0)}}{\partial s} + \sin \phi^{(0)} \cos \phi^{(0)} \left( \frac{\partial u_\theta^{(0)}}{\partial s} - \frac{u_\theta^{(0)}}{R^{(0)}} \frac{\partial R^{(0)}}{\partial s} \right) \\ &+ \frac{\cos^2 \phi^{(0)}}{R^{(0)}} \frac{DR^{(0)}}{Dt}. \end{aligned} \quad (22)$$

See Appendix B for details.

### 3.6. Enforcing constant cell radius and constant wall thickness

It is well-known that cells have negligible growth in the radial direction compared to the axial direction. To enforce this, we invoke the conservation of momentum normal to the wall (16a), which when combined with (22), (17a) and (17c), gives

$$\begin{aligned} \kappa_s^{(0)} \left[ 2\overline{\mu_0} \left( 2 \frac{\partial u_s^{(0)}}{\partial s} + \frac{1}{R^{(0)}} \frac{DR^{(0)}}{Dt} \right) + \left( \overline{\mu_2 a_s^3 a_\theta} + 2\overline{\mu_3 a_s a_\theta} \right) \left( \frac{\partial u_\theta^{(0)}}{\partial s} - \frac{u_\theta^{(0)}}{R^{(0)}} \frac{\partial R^{(0)}}{\partial s} \right) \right. \\ \left. + \overline{\mu_1 a_s^2} + \left( \overline{\mu_2 a_s^4} + 4\overline{\mu_3 a_s^2} \right) \frac{\partial u_s^{(0)}}{\partial s} + \overline{\mu_2 a_s^2 a_\theta^2} \frac{1}{R^{(0)}} \frac{DR^{(0)}}{Dt} \right] \\ + \kappa_\theta^{(0)} \left[ 2\overline{\mu_0} \left( \frac{\partial u_s^{(0)}}{\partial s} + \frac{2}{R^{(0)}} \frac{\partial R^{(0)}}{\partial t} \right) + \left( \overline{\mu_2 a_s a_\theta^3} + 2\overline{\mu_3 a_s a_\theta} \right) \left( \frac{\partial u_\theta^{(0)}}{\partial s} - \frac{u_\theta^{(0)}}{R^{(0)}} \frac{\partial R^{(0)}}{\partial s} \right) \right. \\ \left. + \overline{\mu_1 a_\theta^2} + \overline{\mu_2 a_s^2 a_\theta^2} \frac{\partial u_s^{(0)}}{\partial s} + \left( \overline{\mu_2 a_\theta^4} + 4\overline{\mu_3 a_\theta^2} \right) \frac{1}{R^{(0)}} \frac{DR^{(0)}}{Dt} \right] = P, \end{aligned} \quad (23)$$

where all the quantities with bars above them are defined by (15). From (23), we note that if  $\overline{\mu_2 a_\theta^4} + 4\overline{\mu_3 a_\theta^2} \gg 1$ , meaning that the fibres are highly resistant to extension, then radial changes will be suppressed. We take this condition to be sufficiently strong so that

$$\overline{\mathcal{M}} \equiv \overline{\mu_2 a_\theta^4} + 4\overline{\mu_3 a_\theta^2} \sim \mathcal{O}(\epsilon^{-2}). \quad (24)$$

Assuming (24) and  $P \sim \mathcal{O}(1)$ , we have  $DR^{(0)}/Dt = 0$  and  $DR^{(1)}/Dt = 0$ , which when combined with spatially uniform initial and boundary conditions leads to the solution

$$R^{(0)} = 1, \quad R^{(1)} = 0. \quad (25)$$

From (7) we therefore deduce  $v_s^{(0)} = 0, v_n^{(0)} = 0, v_\theta^{(0)} = 0, v_n^{(1)} = 0$  (the centre surface of the fluid sheet remains stationary), and  $U_s^{(0)} = u_s^{(0)}, U_\theta^{(0)} = u_\theta^{(0)}, U_n^{(0)} = u_n^{(0)} = 0$ . The first-order normal velocity can then be calculated from (A.7) to give

$$u_n^{(1)} = U_n^{(1)} = -\frac{\partial}{\partial s} \left( \left( n + \frac{h^{(0)}}{2} \right) u_s^{(0)} \right). \quad (26)$$

It also follows from (8) that the zeroth-order curvature components are

$$\kappa_\theta^{(0)} = \frac{(1 - (\partial R^{(0)}/\partial s)^2)^{1/2}}{R^{(0)}} = 1, \quad \kappa_s^{(0)} = -\frac{\partial^2 R^{(0)}/\partial s^2}{(1 - (\partial R^{(0)}/\partial s)^2)^{1/2}} = 0, \quad (27)$$

which further implies

$$\overline{\sigma}_{\theta\theta}^{(0)} = P, \quad (28)$$

due to (16a).

Wall thickness is approximately constant during elongation (Dyson et al., 2014). To enforce this condition, we assume that the deposition of new material is calibrated such that the resultant wall thickness  $h^{(0)}$  is constant and uniform, and hence  $h^{(0)} = 1$  by our choice of nondimensionalisation. From (A.6), we require

$$\mathcal{F}^{(1)} = \frac{\partial u_s^{(0)}}{\partial s}. \quad (29)$$

We then find, from (19),

$$\frac{\partial \mu_0^{(0)}}{\partial t} + u_s^{(0)} \frac{\partial \mu_0^{(0)}}{\partial s} - \left( n + \frac{1}{2} \right) \frac{\partial u_s^{(0)}}{\partial s} \frac{\partial \mu_0^{(0)}}{\partial n} = \alpha. \quad (30)$$

and from (21,22),

$$\begin{aligned} \frac{\partial \phi^{(0)}}{\partial t} + u_s^{(0)} \frac{\partial \phi^{(0)}}{\partial s} - \left( n + \frac{1}{2} \right) \frac{\partial u_s^{(0)}}{\partial s} \frac{\partial \phi^{(0)}}{\partial n} \\ = \sin \phi^{(0)} \cos \phi^{(0)} \frac{\partial u_s^{(0)}}{\partial s} - \sin^2 \phi^{(0)} \frac{\partial u_\theta^{(0)}}{\partial s}, \end{aligned} \quad (31)$$

$$\zeta^{(0)} = \sin^2 \phi^{(0)} \frac{\partial u_s^{(0)}}{\partial s} + \sin \phi^{(0)} \cos \phi^{(0)} \frac{\partial u_\theta^{(0)}}{\partial s}. \quad (32)$$

To investigate the interplay between growth and fibre reorientation, we need to relate the fibre angles to the rate of change of elongation and twist. We will derive expressions for the relative elongation and twist rates via integrations along the cell, and kinematic and mechanical balances at the top end. In doing so, we will link the microscopic interactions we have considered in this Section to the emergent macroscopic behaviour of the whole cell.

#### 4. Equations for elongation, twist and fibre reorientation

We proceed to find  $u_s^{(0)}$  and  $u_\theta^{(0)}$  using (16b), (16c) with  $R^{(0)} = 1$ , thus determining the twisting growth behaviour of the cell. We integrate (16b) with respect to  $s$ , and apply a force balance between the tension in the cell wall and the net force due to internal and external pressure on the rigid end plate at  $s = l(t)$ , to find

$$\bar{\sigma}_{ss} = \frac{(P - Q)}{2}, \quad (33)$$

where, from (17a),

$$\bar{\sigma}_{ss} = 4\bar{\mu}_0 \frac{\partial u_s^{(0)}}{\partial s} + \bar{\mu}_1 a_s^2 + \bar{\mu}_2 a_s^2 \zeta + 4\bar{\mu}_3 a_s^2 \frac{\partial u_s^{(0)}}{\partial s} + 2\bar{\mu}_3 a_s a_\theta \frac{\partial u_\theta^{(0)}}{\partial s}. \quad (34)$$

Similarly, integrating (16c) with respect to  $s$ , and imposing the condition that the shear stress at  $s = l$ , the top end of the cell, is equal to the applied torque, we obtain

$$\bar{\sigma}_{s\theta} = \Sigma, \quad (35)$$

where, from (17b),

$$\bar{\sigma}_{s\theta} = \bar{\mu}_0 \frac{\partial u_\theta^{(0)}}{\partial s} + \bar{\mu}_1 a_s a_\theta + \bar{\mu}_2 a_s a_\theta \zeta + \bar{\mu}_3 \frac{\partial u_\theta^{(0)}}{\partial s} + 2\bar{\mu}_3 a_s a_\theta \frac{\partial u_s^{(0)}}{\partial s}. \quad (36)$$

We write (33–36) in the form

$$K_s \frac{\partial u_s^{(0)}}{\partial s} + K_{s\theta} \frac{\partial u_\theta^{(0)}}{\partial s} = T, \quad (37a)$$

$$K_{s\theta} \frac{\partial u_s^{(0)}}{\partial s} + K_\theta \frac{\partial u_\theta^{(0)}}{\partial s} = S, \quad (37b)$$

where

$$K_s = 4\bar{\mu}_0 + \bar{\mu}_2 a_s^4 + 4\bar{\mu}_3 a_s^2, \quad (38a)$$

$$K_\theta = \bar{\mu}_0 + \bar{\mu}_2 a_s^2 a_\theta^2 + \bar{\mu}_3, \quad (38b)$$

$$K_{s\theta} = \bar{\mu}_2 a_s^3 a_\theta + 2\bar{\mu}_3 a_s a_\theta, \quad (38c)$$

represent the averaged directional viscosities and

$$T = \frac{P - Q}{2} - \bar{\mu}_1 a_s^2, \quad (39)$$

$$S = \Sigma - \bar{\mu}_1 a_s a_\theta, \quad (40)$$

are the effective axial tension and azimuthal torque modified by any directional active behaviour of the fibres, respectively. Equations (37a,b) give simultaneous equations for  $\partial u_s^{(0)}/\partial s$  and  $\partial u_\theta^{(0)}/\partial s$ , with solution

$$\frac{\partial u_s^{(0)}}{\partial s} = \frac{TK_\theta - SK_{s\theta}}{K_s K_\theta - K_{s\theta}^2}, \quad (41a)$$

$$\frac{\partial u_\theta^{(0)}}{\partial s} = \frac{SK_s - TK_{s\theta}}{K_s K_\theta - K_{s\theta}^2}. \quad (41b)$$

The right-hand sides of (41a,b) are both independent of  $s$ ; therefore  $u_s^{(0)}$ ,  $u_\theta^{(0)}$  are both linear in  $s$ . Taking  $u_s^{(0)} = 0$  at  $s = 0$ , we can determine the cell length  $l$  by the axial flow velocity at the end of the cell, via  $u_s^{(0)} = dl/dt$  at  $s = l$ . We therefore deduce the relative elongation rate (RER) of the cell, which we denote by  $A$ :

$$\frac{1}{l} \frac{dl}{dt} = \frac{TK_\theta - SK_{s\theta}}{K_s K_\theta - K_{s\theta}^2} \equiv A(P, Q, \Sigma, \mu_0^{(0)}, \mu_{1,2,3}, \phi^{(0)}). \quad (42)$$

This is a Lockhart-type equation (Lockhart, 1965), relating the RER directly to mechanical properties, but here including an additional dependence on fibre angles.

The twist of the cell is related to  $u_\theta^{(0)}$ . Taking  $u_\theta^{(0)} = 0$  on  $s = 0$ , we can calculate the angle of relative twist  $\Theta$  between the top and bottom plates by  $u_\theta^{(0)}(s = l, t) = R^{(0)}d\Theta/dt$ . Therefore, the relative twist rate (RTR) of the cell, denoted by  $B$ , is

$$\frac{1}{l} \frac{d\Theta}{dt} = \frac{SK_s - TK_{s\theta}}{K_s K_\theta - K_{s\theta}^2} \equiv B(P, Q, \Sigma, \mu_0^{(0)}, \mu_{1,2,3}, \phi^{(0)}). \quad (43)$$

The system (38–40) is invariant under the transformation  $\phi \rightarrow \phi + \pi$ , leaving  $K_s, K_\theta, K_{s\theta}, T$  and  $S$  unchanged. However the system does not possess  $\phi \rightarrow -\phi$  invariance, because such a transformation modifies  $K_{s\theta}$  and  $S$ , both of which affect  $A$  and  $B$ . Thus, a reversal of the fibre helicity generally affects both the elongation (through  $A$ ) and twist (through  $B$ ) of the cell, unless  $S = 0$ , in which case the fibre helicity reversal affects only cell twist ( $B \rightarrow -B$ ).

We compute  $\phi^{(0)}$  from (31). Since  $\partial u_s^{(0)}/\partial s$  and  $\partial u_\theta^{(0)}/\partial s$  are independent of  $s$ , if there is no  $s$  dependence in the initial or boundary conditions for  $\phi^{(0)}$ , then no  $s$  dependence can emerge and hence

$$\frac{\partial \phi^{(0)}}{\partial t} - A \left( n + \frac{1}{2} \right) \frac{\partial \phi^{(0)}}{\partial n} = A \sin \phi^{(0)} \cos \phi^{(0)} - B \sin^2 \phi^{(0)}. \quad (44)$$

Recall that  $A, B$  contain integrals across the wall thickness of trigonometric functions of  $\phi^{(0)}$ , and thus (44) is an integro-differential equation. Finally,  $\mu_0^{(0)}$  evolves in time according to (30), which now reads

$$\frac{\partial \mu_0^{(0)}}{\partial t} - A \left( n + \frac{1}{2} \right) \frac{\partial \mu_0^{(0)}}{\partial n} = \alpha, \quad (45)$$

with  $\alpha \geq 0$ . If  $\alpha = 0$ , then  $\mu_0^{(0)}$  is uniformly constant for all time. We discuss initial and boundary conditions for the system in Section 4.1.

To summarise, the complete, simplified system consists of (38–40,42–45). Given appropriate initial and boundary conditions, we solve the system by iterating the following procedure over small timesteps: solve (44) for  $\phi^{(0)}$ , then use (38–40) to compute  $K_s, K_\theta, K_{s\theta}, T, S$  and therefore  $A, B$ , from which the cell length  $l$  is determined via (42), the twist  $\Theta$  is determined via (43), and the isotropic component  $\mu_0^{(0)}$  of matrix viscosity is found by (45). In practice when solving (42) and (43), we replace  $l$  with  $l/l_0$  and  $\Theta$  with  $\Theta/l_0$ , where  $l_0 \equiv l(t=0)$  is the initial cell length. By choice of nondimensionalisation, length is measured in units of cell radius, so  $l_0$  is effectively a physical parameter relating to the initial shape (length:radius ratio) of the cell.

#### 4.1. Initial and boundary conditions

The initial conditions for normalised cell length and twist are  $l(0)/l_0 = 1$  and  $\Theta(0)/l_0 = 0$ . For the fibres, we prescribe initially uniform orientation:  $\phi(n, 0) = \phi_i$  for some  $\phi_i$ , with  $\phi_i = 0$  representing initially transverse fibres. Here,  $\phi_i$  need not be small.

The boundary condition at  $n = 1/2$  is dictated by the choice of fibre-deposition regime, and in this study we investigate two distinct regimes. In both cases, we assume the well-established theory that cortical microtubules guide the deposition of CMF, acknowledging that some studies have cast doubt on the CMF/microtubule co-alignment hypothesis (Himmelsbach et al., 2003; Sugimoto et al., 2003); although, in Section 5 we will reassess that doubt in light of the current model. Following seminal work by Hamant et al. (2008) who established that the orientation of cortical microtubules is determined by the principal stress, we consider a deposition regime whereby new fibres are laid down in alignment with the principal stress direction in the cell wall. Mathematically, given any triad of  $\bar{\sigma}_{ss} = (P - Q)/2$ ,  $\bar{\sigma}_{\theta\theta} = P$  and  $\bar{\sigma}_{s\theta} = \Sigma$ , the principal stress direction  $\phi_{\text{prin}}$  is found by solving

$$\tan(2\phi_{\text{prin}}) = \frac{2\bar{\sigma}_{s\theta}}{\bar{\sigma}_{\theta\theta} - \bar{\sigma}_{ss}} = \frac{4\Sigma}{P + Q}. \quad (46)$$

The fibre-deposition angle  $\phi_b \equiv \phi^{(0)}(1/2, t)$  is then set equal to  $\phi_{\text{prin}}$ :

$$\phi_b = \frac{1}{2} \tan^{-1} \frac{4\Sigma}{P + Q}. \quad (47)$$

This scheme allows  $\phi_b$  to take values in  $-\pi/4 < \phi_b < \pi/4$ . It is known that in certain *Arabidopsis* mutants, microtubules manifest in fixed left- or right-handed arrays (Sedbrook and Kaloriti, 2008); this may be represented by a nonzero constant  $\phi_b$ , concomitant with a fixed, nonzero  $\Sigma$ . The second deposition regime that we will consider is inspired by the experimental observation that, in wild-type *Arabidopsis* roots, cortical microtubules begin rotating out of transverse when cells have moved some distance up the EZ, eventually obtaining oblique orientations (Baskin et al., 2004) or longitudinal ones (Sugimoto et al., 2000). Crucially, the handedness of microtubule reorientation is found to be consistently right-handed. To capture this behaviour, and the assumption that CMF deposition is aligned with the microtubules, we let

$$\phi_b(t) = \frac{2}{3} \left( \tan^{-1} 1 + \tan^{-1} \frac{t - t_0}{t_0} \right), \quad (48)$$

which is a smooth step-function with  $\phi_b(0) = 0$  and  $\phi_b(t) \rightarrow \pi/2$  in the limit  $t \rightarrow \infty$ . The characteristic timescale  $t_0$  on which the variation in  $\phi_b$  occurs is set to  $t_0 = 100$ , so that it coincides with the timescale of large elongation.

Finally, for (45), we prescribe initial condition  $\mu_0^{(0)}(n, 0) = 1$ , and assume that newly deposited wall material has the same initial matrix stiffness as the original cell wall, hence the boundary condition  $\mu_0^{(0)}(1/2, t) = 1$ .

#### 4.2. The parameter space

On the relevant growth timescale, turgor pressure  $P$  and external pressure  $Q$  can be assumed constant. In particular,  $P = 1$  by choice of nondimensionalisation. We also assume the imposed torque  $\Sigma$  to be constant. The prescribed viscosity coefficients  $\mu_{2,3}$ , assumed uniformly constant, must be sufficiently large so that (24) holds for all time. Fibres do not actively exert stress on the system, hence  $\mu_1 = 0$ ; therefore, the effective axial tension  $T = (P - Q)/2$  and azimuthal torque  $S = \Sigma$  are both constant. We let  $\mu_0^{(0)}$  be initially uniform, and either  $\alpha = 0$  so that  $\mu_0^{(0)}$  remains at the initial value, or  $\alpha > 0$  so that  $\mu_0^{(0)}$  evolves spatio-temporally, representing matrix stiffening, where newly deposited material ages as it moves through the wall and reacts with enzymes.

We are interested in elongating cells, so we require that  $A$  is initially positive, which constrains the parameters. The initial denominator of  $A$  is

$$K_s(0)K_\theta(0) - K_{s\theta}(0)^2 = 4\mu_0^{(0)}(0)^2 + 4\mu_0^{(0)}(0) \left[ \mu_3 + \mu_2 a_s(0)^2 a_\theta(0)^2 + \mu_3 a_s(0)^2 \right] + \left[ \mu_0^{(0)}(0)\mu_2 + \mu_2\mu_3 + 4\mu_3^2 \right] a_s(0)^4 > 0. \quad (49)$$

Thus, the numerator of  $A$ , i.e.  $(P - Q)K_\theta/2 - \Sigma K_{s\theta}$ , must also be initially positive. Let us first assume  $P > Q$ . The sign of  $K_{s\theta}(0)$  coincides with the sign of  $\phi_i$ , therefore: if  $\phi_i > 0$  ( $\phi_i < 0$ ), then  $K_{s\theta}(0) > 0$  ( $K_{s\theta}(0) < 0$ ) and so  $\Sigma$  has some positive upper bound (negative lower bound).

We can interpret this property as follows. A positive  $\phi_i$  indicates an initial tendency for the cell to twist left-handedly, or clockwise as seen from the top of the cell (Verger et al., 2019). A positive  $\Sigma$  on the top plate counters this tendency, because it causes anticlockwise elongational flow of the cell wall material as seen from the top. If  $\Sigma$  is sufficiently large, it will cancel out the flow entirely, stifling cell elongation. An analogous analysis applies to the case  $\phi_i < 0$ . It is interesting to note that even if  $P \leq Q$ , i.e. if external longitudinal pressure exceeds turgor, then elongation can still occur due to the effect of the torque  $\Sigma$ , as long as there is some non-transverse initial fibre configuration ( $\phi_i \neq 0$ ), of an appropriate orientation, interacting with the torque. For the remainder of this study, we fix  $Q = 0.5$  so that turgor is greater than the external longitudinal pressure.

## 5. Twist-growth solutions and discussions

In this section, we solve the system numerically and interpret the results in terms of twisting growth. We characterise all growth solutions by the temporal evolutions of fibre angle  $\phi^{(0)}$ , normalised length  $l/l_0$  and normalised twist  $\Theta/l_0$ . Note that if fibres are transverse everywhere for all time, then (42) becomes  $dl/dt \propto Tl$ , implying exponential cell elongation given constant  $T$ . This scenario is modelled by the standard Lockhart equation, so we do not consider it here.

Regardless of fibre-deposition regime and parameter choices, the  $\phi^{(0)}$  solutions exhibit a common property. Initially-present fibres remain uniformly oriented but with an evolving common angle; newly-deposited fibres also re-orient as they are transported through the wall, gaining spatial heterogeneity.

A transition point  $n = N(t)$  separates the two populations of fibres, advecting towards the outer surface over time. We find that  $N(t)$  is related to  $l(t)$  as follows (see Appendix C for details):

$$N(t) = -\frac{1}{2} + \frac{l_0}{l(t)}. \quad (50)$$

Thus,  $N(t)$  is a decreasing function if and only if the cell is elongating.

### 5.1. No matrix stiffening ( $\alpha = 0$ )

We first neglect matrix stiffening, thus setting  $\alpha = 0$ , which implies  $\mu_0^{(0)} = 1$  for all time. Under a constant fibre-deposition angle determined by principal stress, as per equation (47), the evolution of fibre orientations is highly dependent on applied torque  $\Sigma$  and initial fibre angle  $\phi_i$  (Figures 2ab, 3ab). Fibres which are deposited at a positive (negative) angle reorient to larger positive (negative) angles. All the while, initially-present fibres remain transverse if initially transverse, or become more positively or negatively oriented depending on initial orientation. By sampling the orientation angles across the cell wall at a fixed time, we see a  $\phi^{(0)}(n)$  function which is constant for  $-1/2 \leq n < N$ , and smoothly joins the value of  $\phi^{(0)}(1/2) = \phi_b(\Sigma)$  through a ‘kink’. The amplitude of this kink – which represents a sharp variation in fibre angle – grows in time. Note that we do not consider the parameter combination  $(\Sigma, \phi_i) = (0, 0)$ , because it causes fibres to be uniformly transverse for all time and therefore induces exponential elongation.

If all other parameters are fixed while the torque and initial angle are both sign-reversed ( $\Sigma \rightarrow -\Sigma, \phi_i \rightarrow -\phi_i$ ), then the resulting evolution of fibre orientation is also reversed about the horizontal:  $\phi^{(0)}(n, t) \rightarrow -\phi^{(0)}(n, t)$ . This phenomenon can be derived directly from (42–45): when  $\Sigma$  and  $\phi_i$  are sign-reversed,  $A$  is unchanged and  $B$  changes sign, in which case (44) has  $\phi^{(0)} \rightarrow -\phi^{(0)}$  symmetry. Thus,  $\Sigma \rightarrow -\Sigma, \phi_i \rightarrow -\phi_i$  has no effect on the cell elongation, which is determined by  $A$ , and reverses the handedness of cell twist, which is determined by  $B$  (Figures 2cd, 3cd).

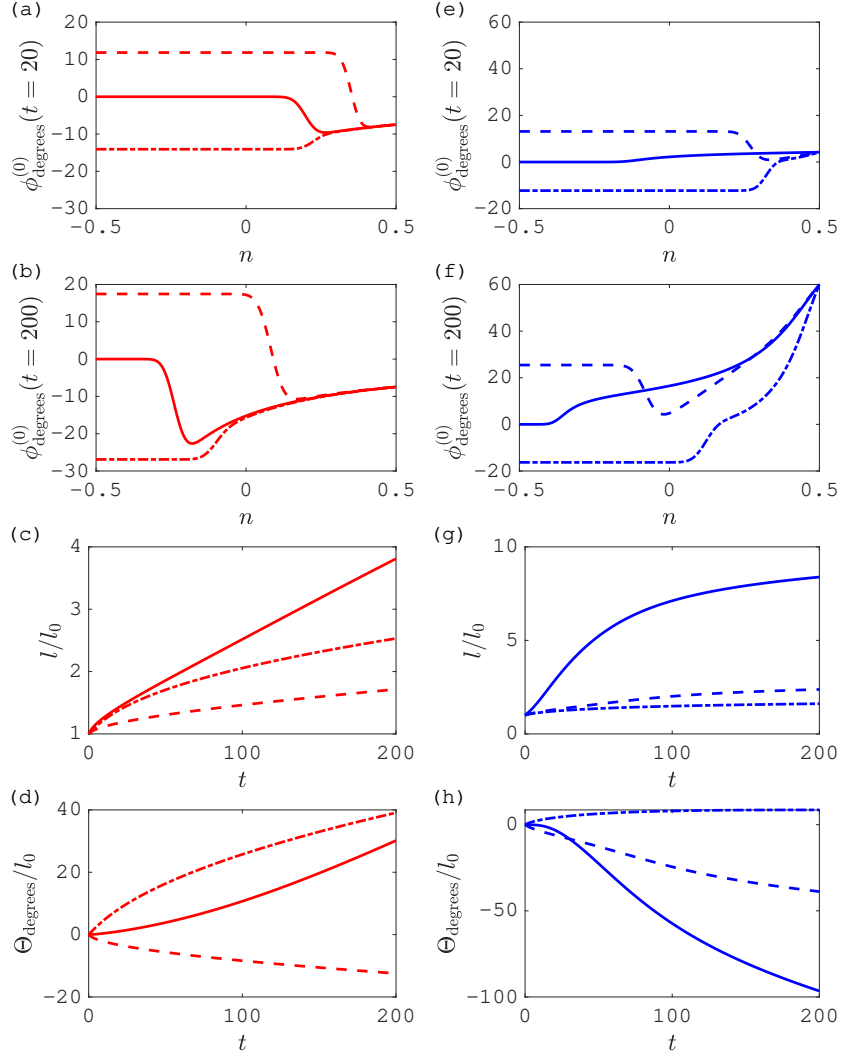


Figure 2: Fibre reorientation visualised as  $\phi^{(0)}(n)$  at different times (a,b,e,f); the corresponding normalised cell length  $l/l_0$  (c,g) and normalised cell twist  $\Theta/l_0$  (d,h) as functions of time. (a)-(d): constant fibre-deposition angle determined by principal stress, as per equation (47). (e)-(f): evolving fibre-deposition angle determined by rotating microtubules, as per equation (48). Parameter values:  $P = 1$ ;  $Q = 0.5$ ;  $\Sigma = -0.1$ ;  $\mu_0 = 1$ ;  $\mu_1 = 0$ ;  $\mu_2 = 100$ ;  $\mu_3 = 1000$ ;  $\alpha = 0$ ; and  $\phi_i = 0^\circ$  (solid lines),  $10^\circ$  (dashed lines),  $-10^\circ$  (dash-dot lines).

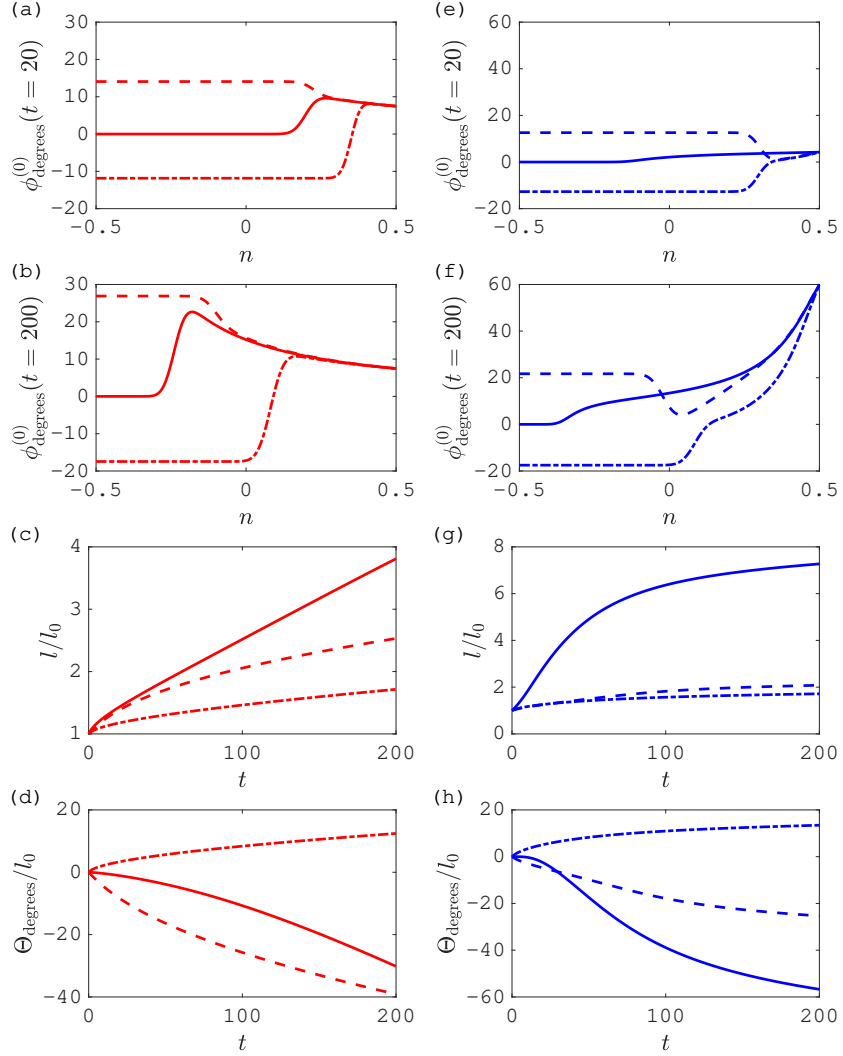


Figure 3: Fibre reorientation visualised as  $\phi^{(0)}(n)$  at different times (a,b,e,f); the corresponding normalised cell elongation  $l/l_0$  (c,g) and normalised cell twist  $\Theta/l_0$  (d,h) as functions of time. (a)-(d): constant fibre-deposition angle determined by principal stress, as per equation (47). (e)-(f): evolving fibre-deposition angle determined by rotating microtubules, as per equation (48). Parameter values:  $P = 1$ ;  $Q = 0.5$ ;  $\Sigma = 0.1$ ;  $\mu_0 = 1$ ;  $\mu_1 = 0$ ;  $\mu_2 = 100$ ;  $\mu_3 = 1000$ ;  $\alpha = 0$ ; and  $\phi_i = 0^\circ$  (solid lines),  $10^\circ$  (dashed lines),  $-10^\circ$  (dash-dot lines).

Given constant-angle deposition (47), if  $\Sigma > 0$  ( $\Sigma < 0$ ) so that  $\phi_b > 0$  ( $\phi_b < 0$ ), and if  $\phi_i \geq 0$  ( $\phi_i \leq 0$ ), then fibres will be oriented at positive (negative) angles throughout the cell wall at all times, forming a right-handed (left-handed) configuration. The corresponding cell twist is always left-handed (right-handed), i.e. towards negative (positive) values of  $\Theta$  (Figures 2d,3d). This behaviour is consistent with the phenomenon that in mutants of *Arabidopsis* which exhibit twisted organ growth, tissue handedness always opposes the handedness of CMT helices in individual cells (we assume that cell twist orientation is consistent with organ twist) (Verger et al., 2019).

Changing the fibre-deposition regime produces significant differences in the model's outputs. Under evolving-angle deposition (48), the fibre configuration is predominantly determined by the deposition angle  $\phi_b(t)$  and initial angle  $\phi_i$ , but not by the applied torque  $\Sigma$ , whose effect on  $\phi^{(0)}(n, t)$  is barely discernible across the range of values  $-0.5 \leq \Sigma \leq 0.5$  (though we only show  $\Sigma = \pm 0.1$  in Figures 2 and 3). In terms of cell elongation, variable deposition causes faster growth initially with slower growth at large times, compared to the same cell under constant, non-zero-angle deposition. This behaviour reflects the fact that  $\phi_b(t)$  is initially close to transverse, so that the entire fibre configuration is initially close to transverse, leading to fast elongation; and that at large times, more and more of the fibres approach a longitudinal orientation, slowing elongation.

If we set  $\Sigma = \phi_i = 0$  (which gave trivial results under constant-deposition), and take the shear viscosity  $\mu_3$  to be very large, we find the following results (Figure 4). At very large times, despite deposited fibres being longitudinal, the majority of fibres in the cell wall are still (nearly) transverse; this is because the very large  $\mu_3$  makes it very difficult for fibres to shear past each other. Deposited fibres therefore mostly remain close to the inner surface of the wall. This behaviour matches experimental observations reported by Sugimoto et al. (2000), that CMF are predominantly transverse throughout the EZ, even though cortical microtubules rotate out of transverse and become longitudinal. The authors interpreted this observation as evidence against the CMF/microtubule alignment hypothesis, but our results here suggest that the hypothesis can still be true despite the mis-alignment of the majority of CMF with microtubules. It is also remarkable that when  $\Sigma = \phi_i = 0$ , the cell twists left-handedly (Figure 4d). This result is coherent with the theory that left-handed cell growth is intrinsically dominant over right-handed cell growth (Landrein et al., 2013; Peaucelle et al., 2015).

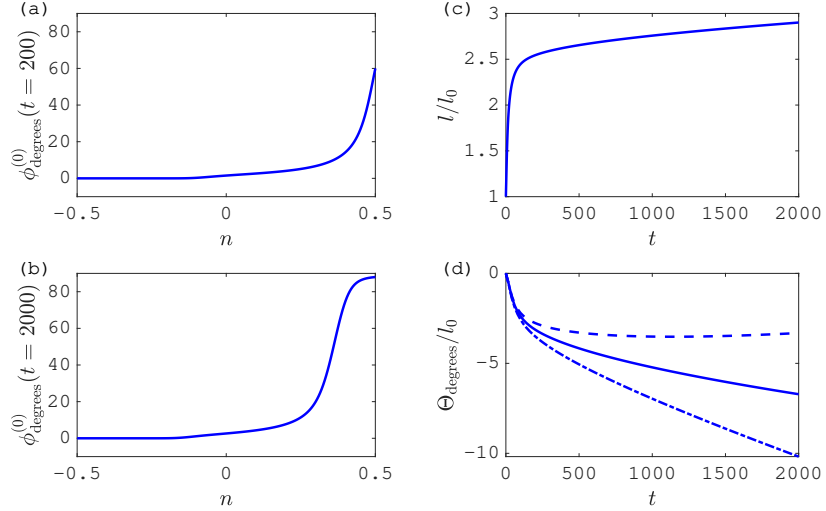


Figure 4: Special case of initially transverse CMF with very large shear viscosity, and an evolving fibre-deposition angle determined by rotating microtubules, as per equation (48). Fibre reorientation visualised as  $\phi^{(0)}(n)$  at different times (a,b); the corresponding normalised cell length  $l/l_0$  (c) and normalised cell twist  $\Theta/l_0$  (d) as functions of time. Parameter values:  $P = 1$ ;  $Q = 0.5$ ;  $\mu_0 = 1$ ;  $\mu_1 = 0$ ;  $\mu_2 = 100$ ;  $\mu_3 = 10^4$ ;  $\alpha = 0$ ;  $\phi_i = 0^\circ$ ; and  $\Sigma = 0$  (solid lines),  $0.1$  (dashed lines),  $-0.1$  (dash-dot lines). The different values of  $\Sigma$  produce identical lines in (a,b,c).

Under the variable-deposition regime of (48), the relationship between elongation and  $\Sigma$  is monotonic (Figure 5ac). If  $\phi_i < 0$  ( $\phi_i > 0$ ), then the speed of growth increases (decreases) with  $\Sigma$ . Meanwhile, cell twist always increases monotonically with  $\Sigma$ , regardless of  $\phi_i$  (Figure 5bd). This trend is present because  $\Sigma > 0$  is a torque that twists the top plate of the cell anticlockwise, which is represented by  $\Theta > 0$ . That is to say, a more positive  $\Sigma$  always makes the cell twist more in the right-handed sense. In comparison, when the fibre deposition angle is constant, as per (47), we see no monotonic relationship between any growth variable and  $\Sigma$ . Instead, there is a value of  $\Sigma = \Sigma_{\text{opt}}$  that maximises elongation, and this value depends on the viscosity parameters as well as on  $\phi_i$  (Figure 5ac). The sign of  $\Sigma_{\text{opt}}$  always coincides with that of  $\phi_i$ . In any case,  $\Sigma_{\text{opt}}$  is an order of magnitude smaller than the other forces  $P$  and  $Q$ .

Not only does  $\Sigma_{\text{opt}}$  maximise elongation, it also maximises the amount of cell twist (Figure 5bd). In other words, a more positive  $\Sigma$  does *not* always make

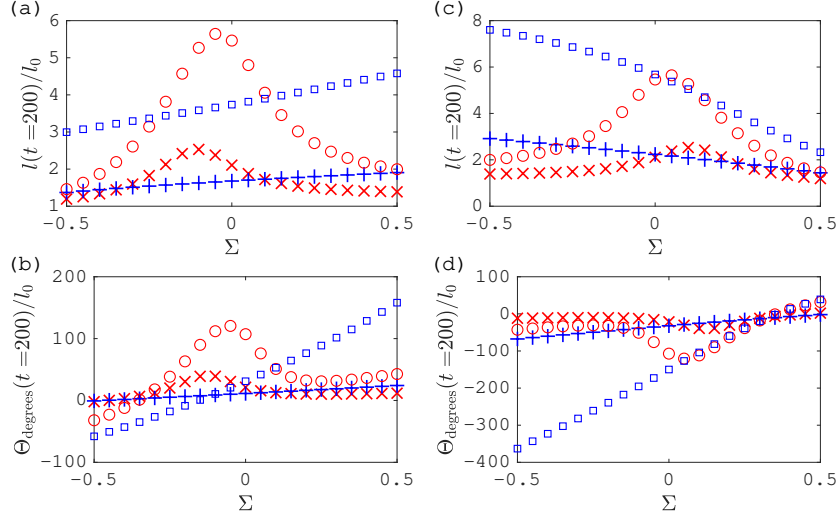


Figure 5: Normalised cell length  $l/l_0$  and normalised cell twist  $\Theta/l_0$  at  $t = 200$ , as functions of  $\Sigma$ , parametrised by  $\phi_i = -10^\circ$  (a,b) and  $\phi_i = 10^\circ$  (c,d). Other parameter values:  $P = 1$ ;  $Q = 0.5$ ;  $\mu_0 = 1$ ;  $\mu_1 = 0$ ;  $\alpha = 0$ .  $(\mu_2, \mu_3) = (100, 1000)$  with constant  $\phi_b$  ('x' markers) and varying  $\phi_b$  ('+' markers);  $(\mu_2, \mu_3) = (1000, 100)$  with constant  $\phi_b$  (circle markers) and varying  $\phi_b$  (square markers).

the cell twist more in the right-handed sense. This result is suggestive of some intrinsic mechanism, which must originate from the coupling of fibre configuration to twist rate, competing with the mechanical function of external torque, i.e. to twist the cell in the direction of  $\Sigma$ . This  $\Sigma$ -resistant mechanism is overridden when the fibre deposition angle varies in time in the specific way we have considered here, which is that it rotates from transverse to longitudinal in a right-handed fashion. The right-handedness of this rotation ‘helps along’ the mechanical effect of  $\Sigma$  to induce twist. Another intrinsic property of the system is that when there is no imposed torque ( $\Sigma = 0$ ), the cell still twists with exactly the handedness that we expect, independent of fibre deposition regime or viscosity parameters: right-handedly (left-handedly) if initial fibre configuration is left-handed (right-handed), i.e. if  $\phi_i < 0$  ( $\phi_i > 0$ ) (Figure 5bd).

## 5.2. Matrix stiffening ( $\alpha > 0$ )

We consider a system with matrix stiffening over time, represented by  $\alpha > 0$ . With initial condition  $\mu_0^{(0)}(n, 0) = 1$  and boundary condition  $\mu_0^{(0)}(1/2, t) = 1$ , we can solve (45) analytically, obtaining an implicit solution for  $\mu_0^{(0)}(n, t)$  and hence an analytic expression for  $\overline{\mu_0}$  valid under the assumption that  $l(t)$  is strictly increasing (see Appendix C for details),

$$\overline{\mu_0(t)} = 1 + \frac{\alpha}{l(t)} \int_0^t l(t') dt'. \quad (51)$$

Thus, the averaged isotropic matrix viscosity is determined by the current cell length and the history of cell elongation up to that time. Since

$$\frac{d\overline{\mu_0}}{dt} = \alpha \left( 1 - \frac{\int_0^t l(t') dt'}{l(t)^2} \right) > 0, \quad (52)$$

$\overline{\mu_0}$  is monotonically increasing in time. In practice, we compute  $\overline{\mu_0}$  using a version of (51) where every instance of  $l$  is replaced by  $l/l_0$ .

In Figure 6, we present results which are typical for an  $\alpha > 0$  system, which is physically identical to figure 3 in all other aspects. With  $\mu_2 = 100$  and  $\alpha = 0.5$ , the  $\mu_0^{(0)}(n, t)$  solution (C.6) dictates that in the region  $n \leq N$  of initially-present wall material,  $\mu_0^{(0)}(n, 200) = 101$ ; in other words, at  $t \approx 200$ , the isotropic matrix viscosity becomes comparable to the extensional viscosity. The most striking finding is the ability of  $\alpha = 0.5$  to suppress cell twist, given an initially transverse fibre configuration  $\phi_i = 0$  (Figure 6dh). Moreover, the correlation between cell twist amount and choice of fibre-deposition regime is significantly reduced by matrix stiffening (see small differences between Figures 6dh versus large differences between Figures 3dh). The matrix stiffening also reduces the correlation between cell elongation and choice of fibre-deposition regime (Figure 6cg versus Figures 3cg).

Overall, the matrix stiffening effect becomes dominant over fibre deposition as the determining factor over the macroscopic growth variables  $l$  and  $\Theta$ , even though changing the deposition regime still has a significant impact on the evolution of fibre configurations in the cell wall (Figure 6abef). In the constant-deposition case, a system with matrix stiffening evolves in such a way that the ‘kink’ in the fibre distribution pushes towards the outer surface of the cell wall more slowly, compared to the system without matrix stiffening

(Figures 6ab versus Figures 3ab). This slowing-down of fibre-reorientation occurs simply because the enlarging isotropic matrix viscosity makes it harder over time for fibres to move in any given direction. As for the varying-deposition case, if fibres are initially transverse, then the matrix stiffening causes the ‘kink’ in the fibre configuration to disappear entirely (Figure 6ef).

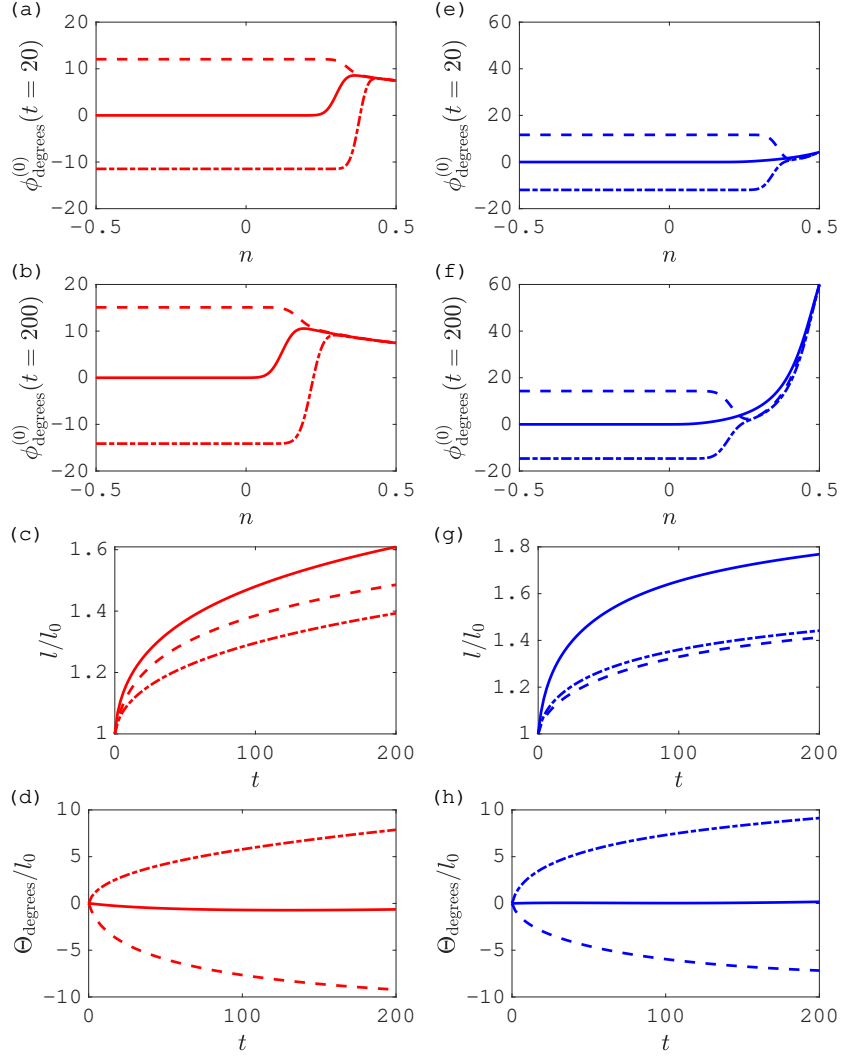


Figure 6: Fibre reorientation visualised as  $\phi^{(0)}(n)$  at different times (a,b,e,f); the corresponding normalised cell length  $l/l_0$  (c,g) and normalised cell twist  $\Theta/l_0$  (d,h) as functions of time. (a)-(d): constant fibre-deposition angle determined by principal stress, as per equation (47). (e)-(f): evolving fibre-deposition angle determined by rotating microtubules, as per equation (48). Parameter values:  $P = 1$ ;  $Q = 0.5$ ;  $\Sigma = 0.1$ ;  $\mu_0 = 1$ ;  $\mu_1 = 0$ ;  $\mu_2 = 100$ ;  $\mu_3 = 1000$ ;  $\alpha = 0.5$ ; and  $\phi_i = 0^\circ$  (solid lines),  $10^\circ$  (dashed lines),  $-10^\circ$  (dash-dot lines).

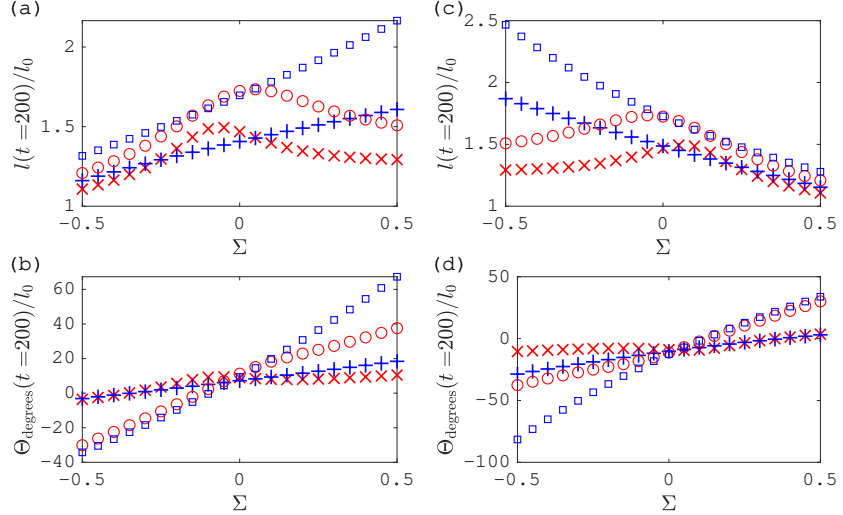


Figure 7: Normalised cell  $l/l_0$  and normalised cell twist  $\Theta/l_0$  at  $t = 200$ , as functions of  $\Sigma$ , parametrised by  $\phi_i = -10^\circ$  (a,b) and  $\phi_i = 10^\circ$  (c,d). Other parameter values:  $P = 1$ ;  $Q = 0.5$ ;  $\mu_0 = 1$ ;  $\mu_1 = 0$ ;  $\alpha = 0.5$ .  $(\mu_2, \mu_3) = (100, 1000)$  with constant  $\phi_b$  ('x' markers) and varying  $\phi_b$  ('+' markers);  $(\mu_2, \mu_3) = (1000, 100)$  with constant  $\phi_b$  (circle markers) and varying  $\phi_b$  (square markers).

With  $\alpha = 0.5$ , a shear viscosity of  $\mu_3 = 1000$  is sufficient for most fibres through the cell wall to remain close to transverse despite new fibres near  $n = 1/2$  becoming nearly longitudinal (Figure 6f). In contrast, a much larger shear viscosity ( $\mu_3 = 10^4$ ) was required to achieve the same effect without stiffening (Section 5.1). This supports our claim that a separation of reorientation dynamics between fibres near the inner wall surface and fibres elsewhere need not invalidate the CMF/microtubule alignment hypothesis.

Figure 7 represents a system which is identical to Figure 5 except for matrix stiffening. For  $\alpha = 0.5$ , cell twist is positively correlated with the applied torque  $\Sigma$  (Figure 7bd); whereas when  $\alpha = 0$ , there exists some optimal  $\Sigma = \Sigma_{\text{opt}}$  inducing the largest amount of cell twist (Figure 5bd). An optimal  $\Sigma$  in terms of inducing the greatest elongation is still observed for  $\alpha = 0.5$  (Figure 7ac); as before, the magnitude of this optimal applied torque is an order smaller than the tension forces.

## 6. Conclusions

We have presented a model to explain twisting plant cell growth using the framework of fibre-reinforced fluid mechanics in the cell wall, with matrix stiffening modelled by a simple transport equation for the isotropic viscosity. Crucially, the model is capable of predicting left-handed and right-handed twisting growth under the same theoretical framework, with different helicities resulting simply from different parameter settings. The deposition of cell wall material is modelled through explicit boundary conditions, including the orientation of new CMF. The fibre-deposition angle is modelled to be either constantly aligned with principal stress (Hamant et al., 2008) or rotating out of transverse towards longitudinal via a prescribed smooth step-function (Sugimoto et al., 2000). In both cases, we have assumed the well-known hypothesis that cortical microtubules guide the deposition of new CMF.

One advantage of explicitly specifying the fibre-angle boundary condition is that it can accommodate any deposition mechanism, even those not involving CMF/microtubule alignment. For example, recent experiments have shown that the cellulose synthases which lay down new CMF simply follow existing synthase tracks when microtubule guidance is disrupted (Chan and Coen, 2020). We can model this situation simply by setting the fibre-deposition equal to the initial fibre angle for all time ( $\phi_b = \phi_i$ ), but still allowing already present fibres to evolve.

We have explained recent experimental findings using this theoretical framework. If the isotropic component  $\mu_0$  of cell wall matrix viscosity remains uniformly constant, with fibre deposition constantly aligned with principal stress, then the model predicts that: (a) reversing both the external torque on the cell and the initial handedness of CMF in the cell wall causes reversal of the handedness of cell twist without affecting cell elongation; (b) the handedness of fibre configurations will remain unchanged over time if it is matched by newly-deposited fibres, in which case the cell grows with the opposite handedness. The latter result is consistent with the recent experimental report by Verger et al. (2019).

On the other hand, if  $\mu_0$  is uniformly constant and the fibre-deposition angle rotates out of transverse over a moderate timescale, then the model predicts that a cell with no applied torque and large shear viscosity in the wall always grows left-handedly. This prediction is consistent with the hypothesis that

cells grow with left-handed twist ‘by default’ (Landrein et al., 2013; Peaucelle et al., 2015). It is also consistent with the theory that when cell-cell adhesion is disrupted (modelled by setting the imposed torque to zero), cells exhibit twisting growth (Verger et al., 2019).

In the model, there usually exists some optimal value of external torque which induces the largest amount of elongation. In the absence of matrix stiffening, this maximum elongation is accompanied by maximum cell twist; however matrix stiffening cancels this twist-maximising effect. If the stiffening coefficient is sufficiently large then it has the effect of suppressing cell twist, resulting in approximately straight growth.

Finally, we found parameter settings (including a large shear viscosity) which produce fibre-reorientation patterns where the majority of CMF remain close to transverse even if the deposition angle has become longitudinal. This effect matches experimental reports (Sugimoto et al., 2000), but raises questions about the authors’ claim that their results invalidate the CMF/microtubule alignment hypothesis.

The novel theoretical framework presented here enables reinterpretation of existing experimental observations about twisting plant cell growth, and reasserts the validity of the CMF/microtubule alignment hypothesis. Furthermore, the framework is sufficiently flexible to test any proposed CMF deposition mechanism, providing a basis on which future experimental results can be explained.

## Acknowledgement

JC and RJD acknowledge support from the EPSRC through Grant No. EP/M00015X/1. JL thanks the University of Birmingham for Post-doctoral Fellowship funding. JC acknowledges valuable discussions with Prof David J. Smith (University of Birmingham).

## Appendix A. Conservation of mass

We expand Eq. (2) in terms of partial derivatives with respect to the co-ordinate variables and use the axisymmetry condition of no variations in the  $\theta$ -direction to obtain

$$\frac{1}{g^{* \frac{1}{2}}} \left\{ \frac{\partial}{\partial s^*} \left( g^{* \frac{1}{2}} U_s^{\sharp*} \right) + \frac{\partial}{\partial n^*} \left( g^{* \frac{1}{2}} U_n^{\sharp*} \right) \right\} = 0, \quad (\text{A.1})$$

where  $g^* = (l_s l_\theta^* l_n)^2$  is the determinant of the metric tensor (see chapter 7 of Aris (1962) for a detailed discussion of expressing divergence in general co-ordinate systems). Here  $U_s^{\sharp*}$  and  $U_n^{\sharp*}$  are the contravariant components of the velocity. Using the relations  $U_s^{\sharp*} = U_s^*/l_s$  and  $U_n^{\sharp*} = U_n^*/l_n$  to rewrite (A.1) in terms of the physical components,  $U_s^*$  and  $U_n^*$ , we obtain

$$\frac{\partial}{\partial s^*} (l_\theta^* U_s^*) + \frac{\partial}{\partial n^*} (l_s l_\theta^* U_n^*) = 0, \quad (\text{A.2})$$

noting that  $l_n = 1$ . We then nondimensionalise (A.2) to obtain

$$\epsilon \frac{\partial}{\partial s} (l_\theta U_s) + \frac{\partial}{\partial n} (l_s l_\theta U_n) = 0, \quad (\text{A.3})$$

where  $u_n = U_n - v_n$  and  $u_s = U_s - v_s$ . Now, expanding Eq. (A.3) and equating terms of equal powers of  $\epsilon$ , we obtain

$$\mathcal{O}(1) : \frac{\partial}{\partial n} (R^{(0)} U_n^{(0)}) = 0, \quad (\text{A.4a})$$

$$\mathcal{O}(\epsilon) : \frac{\partial}{\partial s} (R^{(0)} U_s^{(0)}) + \frac{\partial}{\partial n} \left( l_s^{(1)} R^{(0)} U_n^{(0)} + l_\theta^{(1)} U_n^{(0)} + R^{(0)} U_n^{(1)} \right) = 0. \quad (\text{A.4b})$$

Similarly from (13), we obtain

$$\mathcal{O}(1) : u_n^{(0)} = \begin{cases} -\mathcal{F}^{(0)}, & n = h^{(0)}/2, \\ 0, & n = -h^{(0)}/2, \end{cases} \quad (\text{A.5a})$$

$$\mathcal{O}(\epsilon) : u_n^{(1)} = \begin{cases} -\mathcal{F}^{(1)} + \frac{1}{2} \frac{\partial h^{(0)}}{\partial t} + \frac{1}{2} \frac{\partial h^{(0)}}{\partial s} u_s^{(0)}, & n = h^{(0)}/2, \\ -\frac{1}{2} \frac{\partial h^{(0)}}{\partial t} - \frac{1}{2} \frac{\partial h^{(0)}}{\partial s} u_s^{(0)}, & n = -h^{(0)}/2. \end{cases} \quad (\text{A.5b})$$

Since  $\mathbf{U}^{(0)} = \mathbf{U}^{(0)}(s, t)$  and  $u_n^{(0)} = 0$ , we must therefore have  $\mathcal{F}^{(0)} = 0$ ; unsurprisingly the deposition of new wall material must be the same order of magnitude as the thickness of the wall.

To determine the conservation of mass equation, we need to go to next order. Integrating (A.4b) between the limits  $n = -h^{(0)}/2$  and  $n = h^{(0)}/2$ , and using  $l_s^{(1)} = -\kappa_s^{(0)}n$  and  $l_\theta^{(1)} = R^{(1)} - R^{(0)}\kappa_\theta^{(0)}n$ , we obtain

$$\frac{\partial}{\partial t} (R^{(0)}h^{(0)}) + \frac{\partial}{\partial s} (R^{(0)}h^{(0)}(U_s^{(0)} - v_s^{(0)})) = \mathcal{F}^{(1)}R^{(0)}. \quad (\text{A.6})$$

A similar approach allows us to calculate  $U_n^{(1)}$  which is required to solve (21). Integrating (A.5b) between  $n = -h/2$  and a generic  $n$ , we obtain

$$\begin{aligned} U_n^{(1)} = v_n^{(1)} - \frac{1}{R^{(0)}} & \left( \frac{\partial}{\partial t} (R^{(0)}(n + h^{(0)}/2)) \right. \\ & \left. + \frac{\partial}{\partial s} (R^{(0)}(n + h^{(0)}/2)(U_s^{(0)} - v_s^{(0)})) \right). \end{aligned} \quad (\text{A.7})$$

## Appendix B. Fibre angle evolution equations

We consider the non-dimensionalized version of (6) and expand it in terms of the physical components to obtain, for each  $i$ ,

$$\frac{\partial}{\partial t} \left( \frac{a_i}{l_i} \right) + \sum_j \frac{U_j}{l_j} \frac{\partial}{\partial x_j} \left( \frac{a_i}{l_i} \right) + \zeta \left( \frac{a_i}{l_i} \right) = \sum_j \frac{a_j}{l_j} \frac{\partial}{\partial x_j} \left( \frac{U_i}{l_i} \right). \quad (\text{B.1})$$

Since  $a_n = 0$ , we have that the equation for  $a_s$  is

$$\frac{\partial a_s}{\partial t} - \frac{a_s}{l_s} \frac{\partial l_s}{\partial t} + U_s \frac{\partial}{\partial s} \left( \frac{a_s}{l_s} \right) + \frac{l_s}{l_n} U_n \frac{\partial}{\partial n} \left( \frac{a_s}{l_s} \right) + \zeta a_s = a_s \frac{\partial}{\partial s} \left( \frac{U_s}{l_s} \right). \quad (\text{B.2})$$

We asymptotically expand  $U_i, a_i$  and  $l_i$  in (B.2) to obtain, firstly,

$$\mathcal{O}(1) : \quad U_n^{(0)} \frac{\partial a_s^{(0)}}{\partial n} = 0. \quad (\text{B.3})$$

Then,

$$\mathcal{O}(\epsilon) : \quad \frac{\partial a_s^{(0)}}{\partial t} + U_s^{(0)} \frac{\partial a_s^{(0)}}{\partial s} + U_n^{(0)} \frac{\partial a_s^{(1)}}{\partial n} + U_n^{(1)} \frac{\partial a_s^{(0)}}{\partial n} + \zeta^{(0)} a_s^{(0)} = a_s^{(0)} \frac{\partial U_s^{(0)}}{\partial s}, \quad (\text{B.4})$$

where we have used the fact that  $l_s^{(0)} = 1$ . Similarly the equation for  $a_\theta$  is

$$\begin{aligned} \frac{\partial a_\theta}{\partial t} - \frac{a_\theta}{l_\theta} \frac{\partial l_\theta}{\partial t} + \frac{l_\theta}{l_s} U_s \frac{\partial}{\partial s} \left( \frac{a_\theta}{l_\theta} \right) + \frac{l_\theta}{l_n} U_n \frac{\partial}{\partial n} \left( \frac{a_\theta}{l_\theta} \right) \\ + \zeta a_\theta = \frac{l_\theta}{l_s} a_s \frac{\partial}{\partial s} \left( \frac{U_\theta}{l_\theta} \right), \end{aligned} \quad (\text{B.5})$$

from which we obtain

$$\mathcal{O}(1) : \quad l_\theta^{(0)} U_n^{(0)} \frac{\partial}{\partial n} \left( \frac{a_\theta^{(0)}}{l_\theta^{(0)}} \right) = 0, \quad (\text{B.6})$$

and

$$\begin{aligned} \mathcal{O}(\epsilon) : \quad \frac{\partial a_\theta^{(0)}}{\partial t} - \frac{a_\theta^{(0)}}{l_\theta^{(0)}} \frac{\partial l_\theta^{(0)}}{\partial t} + l_\theta^{(0)} U_s^{(0)} \frac{\partial}{\partial s} \left( \frac{a_\theta^{(0)}}{l_\theta^{(0)}} \right) + l_\theta^{(0)} U_n^{(0)} \frac{\partial}{\partial n} \left( \frac{a_\theta^{(1)}}{l_\theta^{(0)}} \right) \\ + l_\theta^{(0)} U_n^{(1)} \frac{\partial}{\partial n} \left( \frac{a_\theta^{(0)}}{l_\theta^{(0)}} \right) + \zeta^{(0)} a_\theta^{(0)} = l_\theta^{(0)} a_s^{(0)} \frac{\partial}{\partial s} \left( \frac{U_\theta^{(0)}}{l_\theta^{(0)}} \right). \end{aligned} \quad (\text{B.7})$$

Since  $l_\theta^{(0)} = R^{(0)}$ , it follows from (B.7) that

$$\begin{aligned} \frac{\partial a_\theta^{(0)}}{\partial t} + U_s^{(0)} \frac{\partial a_\theta^{(0)}}{\partial s} + U_n^{(0)} \frac{\partial a_\theta^{(1)}}{\partial n} + U_n^{(1)} \frac{\partial a_\theta^{(0)}}{\partial n} + \zeta^{(0)} a_\theta^{(0)} \\ = a_s^{(0)} \left( \frac{\partial U_\theta^{(0)}}{\partial s} - \frac{U_\theta^{(0)}}{R^{(0)}} \frac{\partial R^{(0)}}{\partial s} \right) + \frac{a_\theta^{(0)}}{R^{(0)}} \frac{DR^{(0)}}{Dt}. \end{aligned} \quad (\text{B.8})$$

Using suitable combinations of (B.4) and (B.8), identifying  $a_s^{(0)} = \sin \phi^{(0)}$  and  $a_\theta^{(0)} = \cos \phi^{(0)}$  where  $\phi$  is the fibre angle, we have

$$\begin{aligned} \frac{\partial \phi^{(0)}}{\partial t} + U_s^{(0)} \frac{\partial \phi^{(0)}}{\partial s} + U_n^{(0)} \frac{\partial \phi^{(1)}}{\partial n} + U_n^{(1)} \frac{\partial \phi^{(0)}}{\partial n} = \sin \phi^{(0)} \cos \phi^{(0)} \frac{\partial U_s^{(0)}}{\partial s} \\ - \sin^2 \phi^{(0)} \left( \frac{\partial U_\theta^{(0)}}{\partial s} - \frac{U_\theta^{(0)}}{R^{(0)}} \frac{\partial R^{(0)}}{\partial s} \right) - \frac{\sin \phi^{(0)} \cos \phi^{(0)}}{R^{(0)}} \frac{DR^{(0)}}{Dt}, \end{aligned} \quad (\text{B.9})$$

$$\begin{aligned} \zeta^{(0)} = \sin^2 \phi^{(0)} \frac{\partial U_s^{(0)}}{\partial s} + \sin \phi^{(0)} \cos \phi^{(0)} \left( \frac{\partial U_\theta^{(0)}}{\partial s} - \frac{U_\theta^{(0)}}{R^{(0)}} \frac{\partial R^{(0)}}{\partial s} \right) \\ + \frac{\cos^2 \phi^{(0)}}{R^{(0)}} \frac{DR^{(0)}}{Dt}. \end{aligned} \quad (\text{B.10})$$

## Appendix C. Analytical expressions for $N(t)$ and $\bar{\mu}_0$

Consider characteristic curves in the  $n$ - $t$  space,

$$\frac{dn}{dt} = -A \left( n + \frac{1}{2} \right). \quad (\text{C.1})$$

Along these curves, (45) is equivalent to

$$\frac{d\mu_0^{(0)}}{dt} = \alpha. \quad (\text{C.2})$$

Now, (C.1) has two families of solutions. The first family,

$$n + \frac{1}{2} = \left( n_0 + \frac{1}{2} \right) \exp \left( - \int_0^t A dt' \right), \quad (\text{C.3})$$

emanates from the  $n$ -axis and is parametrised by  $n_0$ . The second family,

$$n + \frac{1}{2} = \exp \left( - \int_{t_0}^t A dt' \right), \quad (\text{C.4})$$

stems from the the line  $n = 1/2$  and is parametrised by  $t_0$ . The two families share a common curve, which we find by setting either  $n_0 = 1/2$  in (C.3) or  $t_0 = 0$  in (C.4), yielding  $n = -1/2 + \exp(-\int_0^t A dt') \equiv N$ . Thus, the  $n$ - $t$  space is divided into two regions by the  $N(t)$  curve. From  $\int_0^t A dt' = \int_0^t \frac{1}{l} \frac{dl}{dt'} dt' = \ln l(t) - \ln l(0)$ , it follows that

$$N(t) = -\frac{1}{2} + \frac{l_0}{l(t)}, \quad (\text{C.5})$$

where  $l_0/l(t) < 1$  is a decreasing function of  $t$  as long as the cell is growing. In each region of the  $n$ - $t$  space, solving (C.2) subject to either the initial or boundary condition is trivial. The result is

$$\mu_0^{(0)}(n, t) = \begin{cases} \alpha t + 1, & n \leq N(t), \\ \alpha(t - t_0(n, t)) + 1, & n > N(t), \end{cases} \quad (\text{C.6})$$

where  $t_0(n, t) \leq t$  is the time at which  $l(t_0) = (n + \frac{1}{2})l(t)$ . Thus, the evolution of  $\mu_0^{(0)}$  can be described as follows. Within an outer region given by

$-1/2 \leq n \leq -1/2 + N$ ,  $\mu_0^{(0)}$  is uniform in space and increases linearly in time with proportionality  $\alpha$ ; in the inner region,  $-1/2 + N < n \leq 1/2$ ,  $\mu_0^{(0)}$  varies in space, decaying monotonically from  $\mu_0^{(0)}(N(t), t)$  to the boundary value of 1.

As long as  $l$  grows strictly monotonically, then there is an analytical expression for  $\bar{\mu}_0 \equiv \int_{-1/2}^{1/2} \mu_0^{(0)} \, dn$ , which is the only form in which  $\mu_0^{(0)}$  appears in our growth equations. We have

$$\int_{-1/2}^{1/2} \mu_0^{(0)} \, dn = (\alpha t + 1) - \alpha \int_N^{\frac{1}{2}} l^{\text{inv}} \left( (n + \frac{1}{2})l(t) \right) \, dn, \quad (\text{C.7})$$

where  $l^{\text{inv}}$ , the inverse function of  $l$ , is well-defined if  $l$  is strictly monotonic. Using the bijective change of variables  $y = (n + \frac{1}{2})l(t)$  (where  $t$  is treated as a constant as far as the integral in (C.7) is concerned), and a theorem concerning the integral of inverse functions (Key, 1994), we deduce

$$\begin{aligned} \bar{\mu}_0 &= (\alpha t + 1) - \frac{\alpha}{l(t)} \int_{l_0}^{l(t)} l^{\text{inv}}(y) \, dy \\ &= (\alpha t + 1) - \frac{\alpha}{l(t)} [y l^{\text{inv}}(y)]_{y=l_0}^{y=l(t)} + \frac{\alpha}{l(t)} \left[ \int_0^{l^{\text{inv}}(y)} l(t') \, dt' \right]_{y=l_0}^{y=l(t)} \\ &= 1 + \frac{\alpha}{l(t)} \int_0^t l(t') \, dt'. \end{aligned} \quad (\text{C.8})$$

## References

Ali, O., Mirabet, V., Godin, C., Traas, J., 2014. Physical models of plant development. *Annual Review of Cell and Developmental Biology* 30, 59–78. doi:10.1146/annurev-cellbio-101512-122410.

Anderson, C.T., Carroll, A., Akhmetova, L., Somerville, C., 2010. Real-time imaging of cellulose reorientation during cell wall expansion in *Arabidopsis* roots. *Plant Physiology* 152, 787–796. doi:10.1104/pp.109.150128.

Aris, R., 1962. *Vectors, Tensors, and the Basic Equations of Fluid Mechanics*. Prentice-Hall, London.

Baskin, T., Beemster, G., Judy-March, J., Marga, F., 2004. Disorganization of cortical microtubules stimulates tangential expansion and reduces the uniformity of cellulose microfibril alignment among cells in the root of *Arabidopsis*. *Plant Physiology* 135, 2279–2290. doi:10.1104/pp.104.040493.

Baskin, T.I., 2005. Anisotropic expansion of the plant cell wall. *Annu. Rev. Cell Dev. Biol.* 21, 203–222. doi:10.1146/annurev.cellbio.20.082503.103053.

Boudaoud, A., 2003. Growth of walled cells: from shells to vesicles. *Physical Review Letters* 91, 018104. doi:10.1103/PhysRevLett.91.018104.

Bruce, D.M., 2003. Mathematical modelling of the cellular mechanics of plants. *Philosophical Transactions of the Royal Society of London B* 358, 1437–1444. doi:10.1098/rstb.2003.1337.

Buschmann, H., Borchers, A., 2019. Handedness in plant cell expansion: a mutant perspective on helical growth. *New Phytologist* 225, 53–69. doi:10.1111/nph.16034.

Chan, J., Coen, E., 2020. Interaction between autonomous and microtubule guidance systems controls cellulose synthase trajectories. *Current Biology* 30, 941–947. doi:10.1016/j.cub.2019.12.066.

Chen, L., Higashitani, A., Suge, H., Takeda, K., Takahashi, H., 2003. Spiral growth and cell wall properties of the gibberellin-treated first internodes in the seedlings of a wheat cultivar tolerant to deep-sowing conditions. *Physiologia Plantarum* 118, 147–155. doi:10.1034/j.1399-3054.2003.00093.x.

Dumais, J., Shaw, S.L., Steele, C.R., Long, S.R., Ray, P.M., 2006. An anisotropic-viscoplastic model of plant cell morphogenesis by tip growth. *The International Journal of Developmental Biology* 50, 209–222. doi:10.1387/ijdb.052066jd.

Dyson, R., Green, J., Whiteley, J., Byrne, H., 2016. An investigation of the influence of extracellular matrix anisotropy and cell-matrix interactions on tissue architecture. *Journal of Mathematical Biology* 72, 17751809. doi:10.1007/s00285-015-0927-7.

Dyson, R.J., Band, L.R., Jensen, O.E., 2012. A model of crosslink kinetics in the expanding plant cell wall: Yield stress and enzyme action. *Journal of Theoretical Biology* 307, 125–136. doi:10.1016/j.jtbi.2012.04.035.

Dyson, R.J., Jensen, O.E., 2010. A fibre-reinforced fluid model of anisotropic plant cell growth. *Journal of Fluid Mechanics* 655, 472–503. doi:10.1017/S002211201000100X.

Dyson, R.J., Vizcay-Barrena, G., Band, L.R., Fernandes, A.N., French, A.P., Fozard, J.A., Hodgman, T.C., Kenobi, K., Pridmore, T.P., Stout, M., Wells, D.M., Wilson, M.H., Bennett, M.J., Jensen, O.E., 2014. Mechanical modelling quantifies the functional importance of outer tissue layers during root elongation and bending. *New Phytologist* 202, 1212–1222. doi:10.1111/nph.12764.

Erickson, J., 1960. Transversely isotropic fluids. *Colloid & Polymer Science* 173, 117–122. doi:10.1007/BF01502416.

van de Fliert, B.W., Howell, P.D., Ockendon, J.R., 1995. Pressure-driven flow of a thin viscous sheet. *Journal of Fluid Mechanics* 292, 359–376. doi:10.1017/S002211209500156X.

Geitmann, A., Ortega, J.K., 2009. Mechanics and modeling of plant cell growth. *Trends in Plant Science* 14, 467–478. doi:10.1016/j.tplants.2009.07.006.

Goriely, A., Tabor, M., 2008. Mathematical modeling of hyphal tip growth. *Fungal Biology Reviews* 22, 77–83. doi:10.1016/j.fbr.2008.05.001.

Green, J.E.F., Friedman, A., 2008. The extensional flow of a thin sheet of incompressible, transversely isotropic fluid. *European Journal of Applied Mathematics* 19, 225–257. doi:10.1017/S0956792508007377.

Hamant, O., Heisler, M.G., Jonsson, H., Krupinski, P., Uyttewaal, M., Bokov, P., Corson, F., Sahlin, P., Boudaoud, A., Meyerowitz, E.M., Couder, Y., Traas, J., 2008. Developmental patterning by mechanical signals in *Arabidopsis*. *Science* 322, 1650–1655. doi:10.1126/science.1165594.

Himmelsbach, R., Williamson, R., Wasteneys, G., 2003. Cellulose microfibril alignment recovers from dcb-induced disruption despite microtubule disorganization. *The Plant Journal* 36, 565–575. doi:10.1046/j.1365-313X.2003.01906.x.

Holloway, C.R., Cupples, G., Smith, D.J., Green, J.E.F., Clarke, R.J., Dyson, R.J., 2018. Influences of transversely isotropic rheology and translational diffusion on the stability of active suspensions. *Royal Society open science* 5, 180456. doi:10.1098/rsos.180456.

Howell, P.D., 1994. Extensional thin layer flows. Dphil thesis. University of Oxford.

Huang, R., Becker, A.A., Jones, I.A., 2012. Modelling cell wall growth using a fibre-reinforced hyperelastic-viscoplastic constitutive law. *Journal of the Mechanics and Physics of Solids* 60, 750–783. doi:10.1016/j.jmps.2011.12.003.

Huang, R., Becker, A.A., Jones, I.A., 2015. A finite strain fibre-reinforced viscoelasto-viscoplastic model of plant cell wall growth. *Journal of Engineering Mathematics* 95, 121–154. doi:10.1007/s10665-014-9761-y.

Jensen, O.E., Fozard, J.A., 2015. Multiscale models in the biomechanics of plant growth. *Physiology* 30, 159–166. doi:10.1152/physiol.00030.2014.

Key, E., 1994. Disks, shells, and integrals of inverse functions. *The College Mathematics Journal* 25, 136–138. doi:10.2307/2687137.

Landrein, B., Lathe, R., Bringmann, M., Vouillot, C., Ivakov, A., Boudaoud, A., Persson, S., Hamant, O., 2013. Impaired cellulose synthase guidance

leads to stem torsion and twists phyllotactic patterns in arabidopsis. *Current Biology* 23, 895–900. doi:10.1016/j.cub.2013.04.013.

Lockhart, J.A., 1965. An analysis of irreversible plant cell elongation. *J. Theor. Biol.* 8, 264–275. doi:10.1016/0022-5193(65)90077-9.

Lynch, J.P., Wojciechowski, T., 2015. Opportunities and challenges in the subsoil: pathways to deeper rooted crops. *Journal of Experimental Botany* 66, 2199–2210. doi:10.1093/jxb/eru508.

Mirabet, V., Das, P., Boudaoud, A., Hamant, O., 2011. The role of mechanical forces in plant morphogenesis. *Annual Review of Plant Biology* 62, 365–385. doi:10.1146/annurev-arplant-042110-103852.

Ortega, J.K.E., 1985. Augmented growth equation for cell-wall expansion. *Plant Physiology* 79, 318–320. doi:10.1104/pp.79.1.318.

Ortega, J.K.E., Welch, S.W.J., 2013. Mathematical models for expansive growth of cells with walls. *Mathematical Modelling of Natural Phenomena* 8, 35–61. doi:10.1051/mmnp/20138404.

Passioura, J.B., Fry, S.C., 1992. Turgor and cell expansion: Beyond the Lockhart equation. *Australian Journal of Plant Physiology* 19, 565–576. doi:10.1071/PP9920565.

Peaucelle, A., Wightman, R., Höfte, H., 2015. The control of growth symmetry breaking in the arabidopsis hypocotyl. *Current Biology* 25, 1746–1752. doi:10.1016/j.cub.2015.05.022.

Saffer, A., Carpita, N., Irish, V., 2017. Rhamnose-containing cell wall polymers suppress helical plant growth independently of microtubule orientation. *Current Biology* 27, 2248–2259. doi:10.1016/j.cub.2017.06.032.

Schulgasser, K., Witztum, A., 2004. The hierarchy of chirality. *Journal of theoretical biology* 230, 281–288. doi:10.1016/j.jtbi.2004.05.012.

Sedbrook, J., Kaloriti, D., 2008. Microtubules, maps and plant directional cell expansion. *Trends in plant science* 13, 303–310. doi:10.1016/j.tplants.2008.04.002.

Smithers, E.T., Luo, J., Dyson, R.J., 2019. Mathematical principles and models of plant growth mechanics: from cell wall dynamics to tissue morphogenesis. *Journal of experimental botany* 70, 3587–3600. doi:10.1093/jxb/erz253.

Somerville, C., Bauer, S., Brininstool, G., Facette, M., Hamann, T., Milne, J., Osborne, E., Paredez, A., Persson, S., Raab, T., Vorwerk, S., Youngs, H., 2004. Toward a systems approach to understanding plant cell walls. *Science* 306, 2206–2211. doi:10.1126/science.1102765.

Sugimoto, K., Himmelsbach, R., Williamson, R., Wasteneys, G., 2003. Mutation or drug-dependent microtubule disruption causes radial swelling without altering parallel cellulose microfibril deposition in arabidopsis root cells. *The Plant Cell* 15, 1414–1429. doi:10.1105/tpc.011593.

Sugimoto, K., Williamson, R., Wasteneys, G., 2000. New techniques enable comparative analysis of microtubule orientation, wall texture, and growth rate in intact roots of Arabidopsis. *Plant physiology* 124, 1493–1506. doi:10.1104/pp.124.4.1493.

Verger, S., Liu, M., Hamant, O., 2019. Mechanical conflicts in twisting growth revealed by cell-cell adhesion defects. *Frontiers in Plant Science* 10, 173. doi:10.3389/fpls.2019.00173.

Veytsman, B.A., Cosgrove, D.J., 1998. A model of cell wall expansion based on thermodynamics of polymer networks. *Biophysical Journal* 75, 2240–2250. doi:10.1016/S0006-3495(98)77668-4.